buildings

MDPI

Article

Cause Investigation of Fractures in the Anti-Arc Portion of the Gravity Dam's Overflow and the Top of the Substation Tunnel

Wenwen Liang [1,*], Lingye Leng [1], Hao Tian [2], Xiao Tian [3] and Caihong Zhang [4,*]

[1] College of Urban Construction, Jiangxi University of Technology, Nanchang 330098, China
[2] China Design Group Co., Ltd., Nanjing 210014, China
[3] Wuhan Ship Communication Research Institute, Wuhan 430205, China
[4] China Construction Seventh Engineering Division Corp. Ltd., Zhengzhou 450012, China
* Correspondence: th2lww@163.com (W.L.); just_only555@163.com (C.Z.); Tel.:+86-136-9954-1286 (W.L.); +86-136-6932-1618 (C.Z.)

Abstract: Clarifying the origins of fractures and adopting acceptable repair plans are crucial for the design, maintenance, and safe operation of concrete gravity dams. In this research, numerical simulation is largely utilized to investigate the reasons for fractures in the anti-arc portion of the concrete gravity dam and the top of a substation tunnel in Guangdong Province, China. The calculation parameters are chosen based on the design information and engineering expertise to model the temperature field and stress field distribution of the dam during both normal operation and severe weather. The study demonstrates that under the effect of severe structural restraints and high temperatures, the tensile stress at the top of the substation tunnel would be 2.64 MPa in the summer, which is more than the tensile strength by 1.5 MPa and causes deep cracks. The tensile stress reaches 3.0 MPa in the summer under the effect of severe weather near the top of the substation tunnel. When a cold wave strikes in the winter, the concrete's tensile stress on the overflow dam surface rises from 1.6 MPa to 4.0 MPa, exceeding the tensile strength by 1.9 MPa, resulting in the formation of a connection fracture in the reverse arc section. Both the actual observed crack location and the monitoring findings of the crack opening, as determined by the crack gauge, agree with the modeling results. The technique to lessen the structural restrictions of a comparable powerhouse hydropower station is pointed out based on engineering expertise, and various and practical repair strategies are proposed to guarantee the structure's safe operation.

Keywords: concrete gravity dam; causes of cracks; thermal stress; numerical simulation; repair scheme

check for updates

Citation: Liang, W.; Leng, L.; Tian, H.; Tian, X.; Zhang, C. Cause Investigation of Fractures in the Anti-Arc Portion of the Gravity Dam's Overflow and the Top of the Substation Tunnel. *Buildings* **2023**, *13*, 1531. https://doi.org/10.3390/buildings13061531

Academic Editor: Panagiotis Stylianidis

Received: 17 May 2023
Revised: 8 June 2023
Accepted: 13 June 2023
Published: 15 June 2023

1. Introduction

The gravity dam meets its own stability criteria by creating its own anti-sliding force. It has been extensively employed as a result of its comparatively high levels of safety and dependability, excellent durability, simple design and construction methods, and robust terrain and geological condition adaptability [1,2]. Concrete or grouted rubble was used to build the gravity dam's portion, which is essentially triangular. Large-scale operations involving the management of water often use concrete gravity dams.

However, cracks are a common occurrence in concrete dams, which negatively impact the dam's economic benefits and safe operation and even increase the risk of accidents. Due to the exothermic hydration reaction of concrete, thermal gradients are created during construction. At the same time, because of the creep and autogenous volume shrinkage properties of concrete materials, it is simple to create large thermal stresses that are greater than the tensile strength of concrete and result in temperature cracks [3,4]. The concrete dam will also produce greater tensile stress during the structure's operational period due to seasonal temperature variations [5], foundation settlement, overloading [6], sudden earthquakes [7,8], flood discharge, etc. If this stress exceeds the tensile strength of concrete, it will also result in cracks. These cracks destroy the integrity of the structure and affect its stiffness, thus reducing its bearing capacity [9,10]. Additionally, the presence of fractures worsens the leakage channel and reduces the dam's ability to store water and provide benefits. Additionally, the existence of cracks provides a leakage channel, which affects the water storage performance and benefits of the dam. These leakage channels also serve as an erosive pathway for corrosive substances, which speeds up the corrosion of steel bars in concrete. The expansion of corrosion products further intensifies concrete cracking, which significantly reduces the structure's durability and fails to reach its design service life. Under special loads, such as earthquakes, cracks in concrete dams will expand rapidly, leading to structural damage [7].

The service conditions of concrete are complex, and the load types are diverse, so it is necessary to strengthen the monitoring of cracks during construction and operation. At present, many methods have been developed for crack monitoring, such as point strain sensors: strain gauges [11], vibrating wire sensors [12], fiber Bragg-grating sensors [13], photogrammetry [14], laser scanning [15], and other surface detection methods. Xiao Tan et al. [16] presents a method to measure and visualize strains and cracks in concrete using distributed fiber optic sensors based on optical frequency domain reflectometry. Effective detection is crucial to safeguarding the safety of hydraulic infrastructure like dams since it relates to the security of the national water network. In addition to the traditional manual detection method [17], Yantao Zhu et al. [18] put forward the automatic detection and diagnosis technology of hydraulic structure damage based on drones and artificial intelligence techniques to ensure the safe operation of the dam. Predicting dam deformations based on monitoring data is also crucial. Traditional statistical model techniques like linear regression [19] and neural network techniques [20] are among the prediction techniques.

Due to the complex service environment and the impact of diverse loads, it would be challenging to identify the causes of cracks in concrete dams after they have been identified. Currently, the main methods used to investigate the causes of dam cracks are numerical simulation [21], engineering experience [22], and physical model testing [23,24]. The failure of the law of gravity dam may be partially reflected by a physical model test. However, because the crack opening in the dam body in real engineering is only a few centimeters larger than in the model, it is challenging to track the crack's development and adhere to the similarity law's requirements. Additionally, a model test has a lengthy experimental period, high cost, and weak applicability. Based on engineering expertise, it is fast and easy to guess the origins of fractures, although there may be variations because of a lack of theoretical foundation. Additionally, since each dam's causes vary, a specific analysis is necessary that may not follow conventional engineering wisdom. Numerical simulation can, on the one hand, cut down on the time and money needed to investigate crack causes; on the other hand, the simulation at this stage has perfect theoretical support, and the simulation results can match the measured data, making it a better method for researching crack causes [25]. Therefore, this paper studies the causes of cracks in concrete gravity dams by numerical simulation.

Temperature change has an important influence on the construction and operation periods of mass concrete. However, only the temperature field and thermal stress of the structure during construction are often taken into account during the design stage of a concrete dam [3,4]. The research on the influence of temperature change on concrete dams during normal operation periods focuses more on arch dams [26] and buttress dams [5], while concrete gravity dams are often ignored. However, this practice is obviously not in line with China's national conditions. The majority of the southeast coast of China has a subtropical monsoon climate with significant yearly temperature variance. There will be a significant temperature differential between the inside and outside of the dam during normal operation, and when it is confined by the structure, there will also be a large thermal stress. The frequent occurrence of severe weather, such as high summer temperatures and heavy rain and harsh winter waves, may increase thermal stress, cause temperature cracks, and jeopardize structural safety as a result of global climate change. However, the influence of extreme weather is often ignored in related research, which is quite inappropriate. Additionally, the majority of studies only conduct superficial analysis and study on the temperature field and stress field simulation findings, which makes it challenging to draw conclusions and serve as a reference point for structural design. Therefore, when crack causes are investigated using numerical modeling, specialized techniques are required to identify the underlying structural reasons of high stress. In addition, the causes are compared with similar structures so as to put forward ways to reduce structural constraints and thermal stress for the design of new concrete gravity dams and put forward suggestions for repairing damaged structures.

The study's three key goals are as follows: (1) To investigate the causes of the cracks at the top of the substation tunnel and the anti-arc portion of the Fengshu Gravity Dam's overflow dam section using numerical simulation and compare the findings with the results of the detection; (2) Research how the temperature field and stress field of the dam are adversely affected by extreme weather; (3) Find out the dam's irrationality and provide examples of other dam structures with a similar design. In order to simulate the distribution of the temperature field and stress field of the dam during normal operation and extreme weather, this paper first chooses the overflow dam section where the cracks are located, creates the finite element model of the dam section, selects reasonable calculation parameters based on the dam design data and engineering experience, and then analyzes the negative effects of extreme weather. The results of the seam gauge monitoring and real observations help to validate the simulation's correctness. The linear expansion coefficient adjustment method is then proposed to adjust the linear expansion coefficient of various structural components in order to analyze the causes of cracks and identify the unreasonable structural components in accordance with the fundamental calculation theory of thermal stress fields. Finally, different repair schemes are compared, feasible, reasonable, and economical crack repair schemes are put forward, and references and suggestions are provided for the design and repair of similar structures.

The remainder of the paper is organized as follows: Section 2 gives the calculation theory referenced by the simulation; Section 3 introduces Fengshuba and gives the calculation model and parameters; Section 4 gives the simulation results and analyzes the causes of cracks and the influence of extreme weather; Section 5 compares other structures and puts forward the repair scheme; and Section 6 summarizes the main research conclusions of this paper.

2. Methodology

According to the monitoring data, the reverse arc substation tunnel's top fracture, which is thought to have been caused by a temperature shift, has not seen apparent displacement or settlement at the dam. In order to understand the reasons behind fractures, the temperature field and stress field in the overflow dam section of a gravity dam will be simulated using finite element numerical simulation in this article. The simulation uses the sequential coupling approach, in which the temperature field distribution of the dam is computed first, while the stress field is subsequently solved using the temperature field's calculation findings.

2.1. Algorithm of Quasi-Stable Temperature Field

At an arbitrary point in the computation domain R, the quasi-stable temperature field $T(x, y, z, \tau)$ must satisfy the heat conduction equation:

$$\nabla^2 T = 0 \tag{1}$$

where T is the temperature of the concrete, (°C).

Comply with the first C or third C' type of boundary condition:

$$\begin{aligned} C:&\quad T = T_a \\ C':&\quad \frac{\partial T}{\partial n} + \frac{\beta}{\lambda}(T - T_a) = 0 \end{aligned} \tag{2}$$

where T_a is the ambient temperature, (°C). β is the surface heat dissipation coefficient, (kJ/(m^2·h·°C)). λ is the thermal diffusivity, (kg/(m·d·°C)). n is the outer normal direction of the boundary.

Through the principle of variation, the functional equation of the temperature field is obtained as:

$$I(T) = \iiint\limits_{R} \left\{ \frac{1}{2} \nabla^2 T \right\} dxdydz + \iint\limits_{C} \left\{ \frac{\beta}{\lambda} \left(\frac{1}{2} T^2 - T_a T \right) \right\} ds \tag{3}$$

The eight-node hexahedral element is used to discretize the computational domain R. By using the classical Galerkin method and Gaussian integral, the integral in discrete domain is calculated, and the calculation formula is obtained.

$$\begin{cases} \left([H] + \frac{1}{\Delta\tau_n}[R] \right) \{T_{n+1}\} - \frac{1}{\Delta\tau_n}[R]\{T_n\} + \{F_{n+1}\} = 0 \\ H_{ij} = \iiint\limits_{\Delta R} \left(\left(B_i^{\phi} \right)^T \left(B_j^{\phi} \right) \right) dxdydz + \iint\limits_{\Delta S} \frac{\beta}{\lambda} N_i N_j ds \\ R_{ij} = \iiint\limits_{\Delta R} \frac{c\rho}{\lambda} \cdot N_i \cdot N_j dxdydz \\ F_i = \iiint\limits_{\Delta R} \frac{\beta}{\lambda} \cdot T_a \cdot N_i dxdydz \\ B_i^{\phi} = [N_{i,x}, N_{i,y}, N_{i,z}]^T \end{cases} \tag{4}$$

where c is specific heat capacity, (kJ/(kg·°C)). ρ is density, (kJ/m^3). $[H]$ is the heat conduction matrix, $[B]$ is the matrix of displacement and strain, N_i is the shape function, $[R]$ is the conduction supplementary matrix, $\{T_n\}$ and $\{T_{n+1}\}$ are the node temperature vector of n and $n+1$ time, respectively, $\{F_{n+1}\}$ is the node temperature load vector. According to Equation (4), $\{T_{n+1}\}$ can be obtained from $\{T_n\}$, where $[H]$ and $[R]$ are invariants in the iteration, and $\{F_{n+1}\}$ is a known quantity in the iteration.

2.2. Algorithm of Stress Field

For the long-term operation of concrete gravity dam, the main creep deformation and autogenous volume deformation have been basically completed, which can be ignored in the calculation, so the influence of external load and temperature change is mainly considered. In order to solve this problem, the strain increment $\{\Delta\varepsilon_n\}$ of the calculation domain in a certain load step mainly includes elastic strain increment $\{\Delta\varepsilon_n^e\}$ and temperature strain increment $\left\{\Delta\varepsilon_n^T\right\}$.

$$\{\Delta\varepsilon_n\} = \{\Delta\varepsilon_n^e\} + \left\{\Delta\varepsilon_n^T\right\} \tag{5}$$

Elastic strain increment $\{\Delta\varepsilon_n^e\}$ may be calculated as:

$$\{\Delta\varepsilon_n^e\} = [D][\Delta\sigma_n] \tag{6}$$

where $\Delta\sigma_n$ is the stress increment, (Pa). $[D]$ is the elastic matrix describing the stress–strain relationship.

The temperature strain increment $\left\{\Delta\varepsilon_n^T\right\}$ is calculated using the following expression from the results of the unsteady temperature field computation:

$$\left\{\Delta\varepsilon_n^T\right\} = \{\alpha\Delta T_n, \alpha\Delta T_n, \alpha\Delta T_n, 0, 0, 0\} \tag{7}$$

where α is the coefficient of linear expansion, (10^{-6}/°C). ΔT_n is the temperature increment during $\Delta\tau_n$.

The calculation area adopts the same calculation unit as the temperature field. The overall balance equation is established according to the principle of virtual work.

$$\begin{cases} [K]\{\Delta\delta_n\} = \{\Delta P^L{}_n\} + \{\Delta P^T{}_n\} \\ [K] = \sum\limits_e \iiint\limits_{\Delta R} [B]^T [D][B]dxdydz \\ \{\Delta P_n\} = \sum\limits_e \iiint\limits_{\Delta R} [B]^T [D]\{\Delta\varepsilon_n\}dxdydz \end{cases} \tag{8}$$

where $[K]$ is the overall stiffness matrix, $\{\Delta\delta_n\}$ is the increment of nodal displacement during $\Delta\tau_n$, $\{\Delta P^L{}_n\}$ is the equivalent nodal force increment by external load during $\Delta\tau_n$, $\{\Delta P^T{}_n\}$ is the equivalent nodal force increment by temperature change.

After the displacement increment is obtained, the node stress increment is calculated by the following formula:

$$[\Delta\sigma_i] = [D] \cdot ([B]\{\Delta\delta_n\} - \left\{\Delta\varepsilon_i^T\right\}) \tag{9}$$

Accumulate the incremental results of each step to obtain displacement (δ_n) and stress (σ_n) at any time:

$$\delta_n = \sum_{i=1}^{n} \Delta\delta_i \quad \sigma_n = \sum_{i=1}^{n} \Delta\sigma_i \tag{10}$$

Through the secondary development of ANSYS, the finite element calculation of mass concrete can be realized. The specific implementation process has been elaborated in the manuscript by Wenqiang Xu et al. [27]. The calculation program can be obtained from the correspondent.

3. Simulation Model and Parameters

3.1. Model of Dam

The focus of this study is Fengshuba, a concrete gravity dam in Heyuan City, Guangdong Province, China. It is situated in the upper sections of the Dongjiang River, a tributary of the Pearl River. The maximum dam height is 95.3 m, the greatest width of the dam bottom is 87.1 m, the longest length of the crest is 418 m, and the highest elevation of the crest is 173.3 m. The dam profile is shown in Figure 1. The dam was built beginning in May 1970; the primary project was finished in 1975; and the dam was finished and approved in August 1983. It serves as a center for water conservation and makes extensive use of shipping, electricity production, and flood control. It is made up of a concrete barrage, a spillway at the top of the dam, a powerhouse and substation within the dam, and pipes used to release water and facilitate water crossing the dam.

Deep cracks were discovered during the 2005 safety inspection in the overflow surface's anti-arc portion, as well as other horizontal cracks at the top of the substation tunnel's overflow dam section. For analysis, a typical overflow dam section is used. According to the finite element model in Figure 2a, the overflow dam section has a height of 79.4 m, lengths of 86.8 m upstream and downstream, and a width of 17 m. The impact of the foundation on the calculation findings is taken into account to assure the correctness of the computation. The foundation's range is 100 m upstream and downstream of the dam, 54 m on each side of the dam, and 150 m below. Figure 2b depicts the total finite element computation model. An eight-node hexahedron element is used for subdivision, with the total number of elements being 67,809 and the total number of nodes being 76,984. The element type in the calculation is Solid 45. Previous studies have shown that the smaller the mesh size, the more accurate the calculation results. In the case of a large temperature gradient change, when the cell size is less than 0.2 m, the calculation results converge and tend to be stable [28]. Considering that the dam surface and the substation tunnel area are easily affected by the outside air temperature, the surface temperature gradient will be large, so the grid of the corresponding area has been refined when meshing. At the same time, cracks appeared in the top and reverse arc sections of the substation tunnel, and the preliminary calculation results also showed that the stress value of this part was larger than that of the rest of the dam because of the unreasonable structural design, so it needed to be paid more attention to and analyzed. Therefore, the mesh of the area near the substation tunnel will also be refined, as shown in Figure 2c.

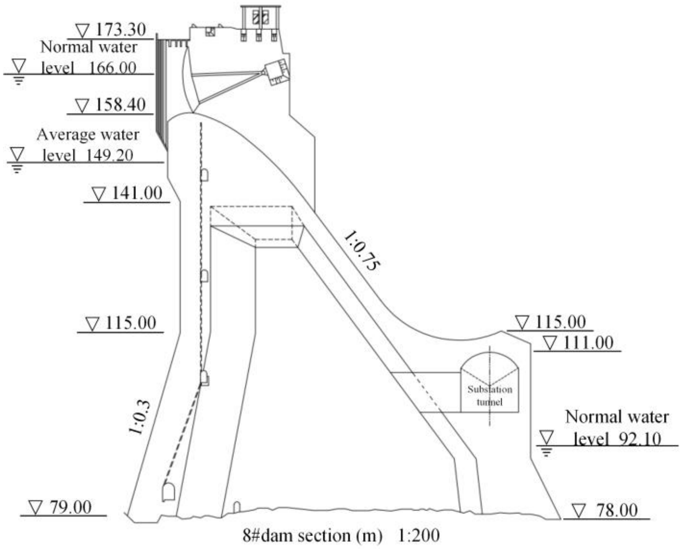

Figure 1. Profile of the dam.

3.2. Simulation Parameters

The thermodynamic characteristics of the concrete and foundation in the overflow dam section are reported in Tables 1 and 2, respectively, based on the dam's design data and relevant technical expertise. Among them, the mechanical parameters of dam concrete, such as elastic modulus and Poisson's ratio, are obtained from the experiment before construction. Thermal parameters, such as thermal conductivity, specific heat, etc., are calculated according to the concrete mix ratio and referring to the research of Zhu Bofang [29]. The mechanical parameters of the foundation are selected according to the survey data. The thermal parameters of rock foundations are calculated and obtained according to the rock types obtained by investigation and referring to the research of Zhu Bofang [29]. Since the dam has been operating for a considerable amount of time, the creep deformation and autogenous volume shrinkage have essentially ended; therefore, they will not be taken into account in the computation.

Table 3 displays the dam site's multi-year monthly average temperature, which Equation (9) fits and uses in the simulation. Figure 3 displays the temperature throughout a multi-year period that was measured, along with its fitting value.

$$T_a(t) = 20.5 + 8.57 \times \cos\left[\frac{\pi}{6}(t - 7.1)\right] \quad (t \quad month) \tag{11}$$

Table 1. Thermodynamic parameters of dam concrete.

Parameters	Symbol	Unit	Value
Density	ρ	kg/m^3	2400
Elastic modulus	E	N/mm^2	2.8×10^4
Poisson's ration	μ		0.167
Linear expansion	α	10^{-6}/°C	8.34
Thermal conductivity	λ_c	kg/(m·d·°C)	8.46
Heat capacity	C_c	kJ/(kg·°C)	0.91

Table 2. Thermodynamic parameters of foundation.

Parameters	Symbol	Unit	Value
Density	ρ	kg/m^3	2780
Elastic modulus	E	N/mm^2	1.5×10^4
Poisson's ration	μ		0.20
Linear expansion	α	$10^{-6}/°C$	7.50
Thermal conductivity	λ_c	kg/(m·d·°C)	6.88
Heat capacity	C_c	kJ/(kg·°C)	0.76

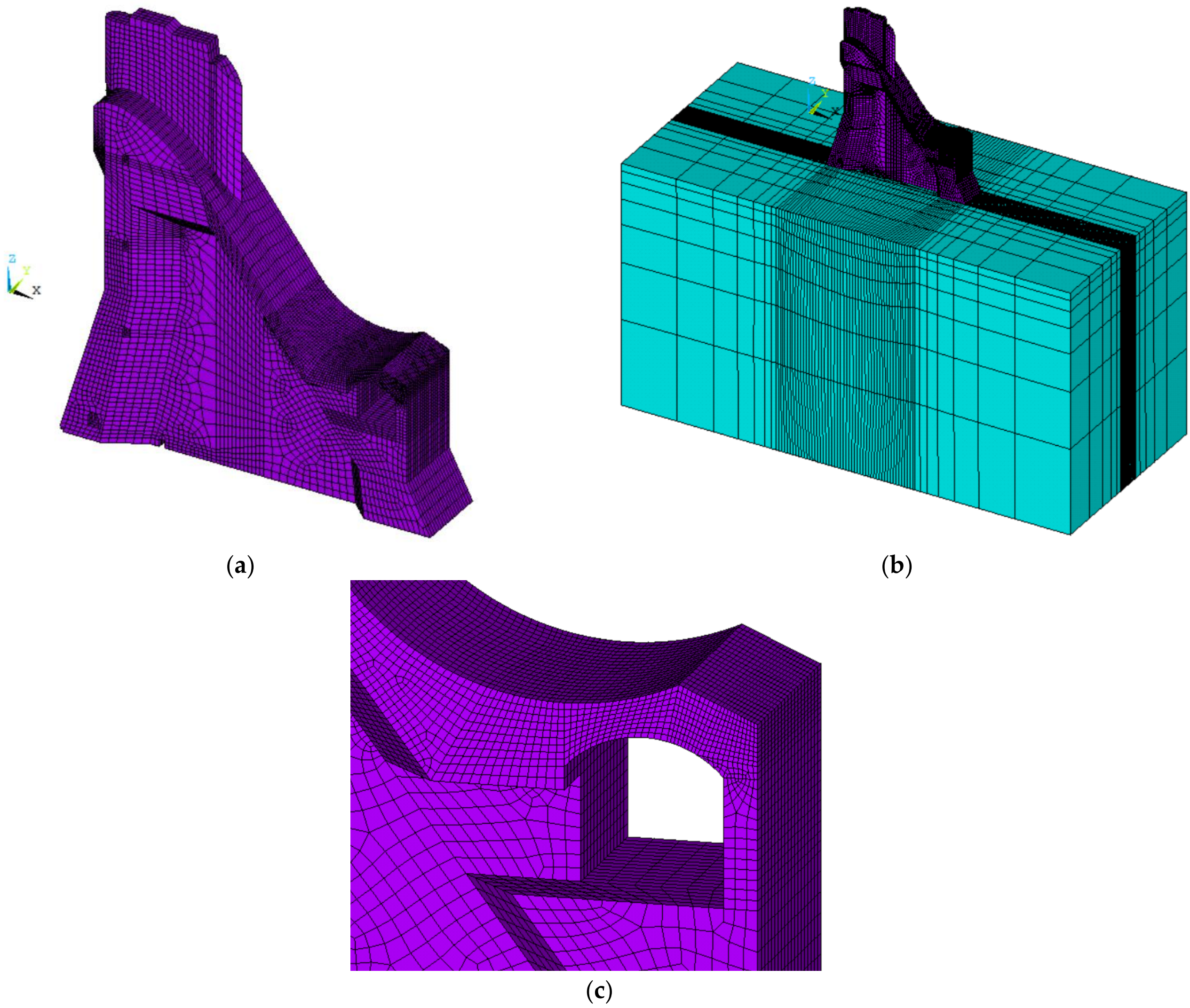

(**a**) (**b**) (**c**)

Figure 2. Finite element calculation model. (**a**) Overflow dam section only, (**b**) Foundation included, (**c**) Area near the substation tunnel.

Table 3. Multi-year monthly average temperature.

Mouth	1	2	3	4	5	6	7	8	9	10	11	12	Average
Temperature/°C	10.6	12.3	16.7	21.2	24.9	26.5	28.1	27.8	26.1	21.9	17.6	12.6	20.5

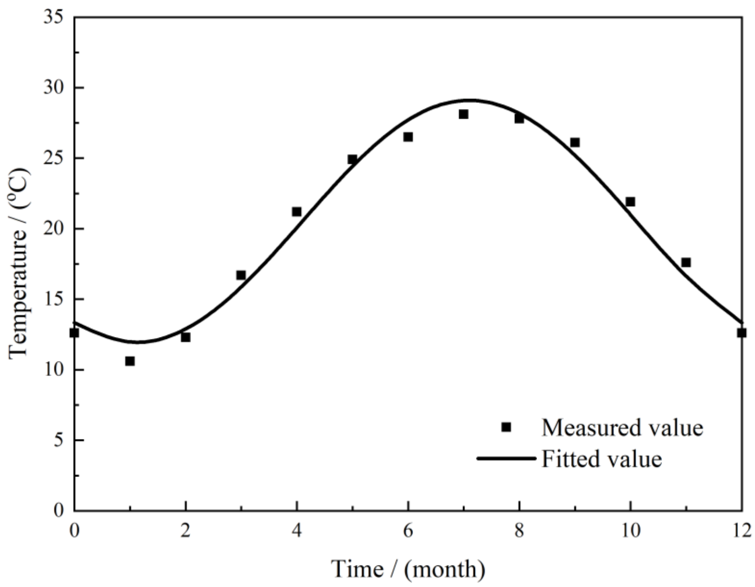

Figure 3. Measured and fitted value of multi-year monthly average temperature.

There is a greenhouse effect since the substation tunnel is within the dam and not in direct touch with the environment outside, which reduces the interior temperature fluctuation. The fitting equation for the interior temperature of the substation tunnel is provided, and it is based on collected data and technical expertise:

$$T_a(t) = 20.5 + 3.0 \times \cos\left[\frac{\pi}{6}(t - 7.1)\right] \quad (t \quad month) \tag{12}$$

The highest water level in front of the dam is 165.53 m, which is lower than the reservoir's normal water level of 166.0 m, according to observation records of water levels in the reservoir. In addition, the dam is in a discharge condition when the water level is at its peak. The lowest water level observed in front of the dam is 125.83 m, which is lower than the dead water level of 128 m. The average water level of each month is shown in Table 4. When calculating, the upstream water level H_w is fitted by Equation (13):

$$H_w(t) = 149.23 + 6.27 \times \cos\left[\frac{\pi}{6}(t - 8.46)\right] \quad (t \quad month) \tag{13}$$

Table 4. Monthly average water level.

Month	1	2	3	4	5	6	7	8	9	10	11	12	Average
Water level/m	144.8	142.6	142.1	144.9	148.0	152.2	154.2	154.5	154.2	153.3	151.4	148.6	149.2

When calculating the temperature field, the reservoir water temperature should be taken into account. The reservoir's water temperature is determined using Zhu Bofang's formula [29] since there is no equipment for measuring the water's temperature there. Equations (14)–(18) compute the water temperature at any depth and any time.

$$T(y, \tau) = T_m(y) + A(y)\cos\left(\frac{\pi}{6}(\tau - \tau_0 - \varepsilon)\right) \tag{14}$$

$$T_m(y) = c + (T_s - c)e^{-0.04y} \tag{15}$$

$$c = (T_b - T_s)/(1 - g), g = e^{-0.04H} = (11 - 23.5)/(1 - e^{-0.04H}) \tag{16}$$

$$A(y) = A_0 e^{-0.018y} = 8.57 \times e^{-0.018y} \tag{17}$$

$$\varepsilon = 2.15 - 1.30e^{-0.085y} \tag{18}$$

where $T(y, \tau)$ is the temperature of the water depth y at the time τ, (°C). y is the water depth, (m). τ it is time, (month). τ_0 is the time with the highest temperature, which is 7.1 in the calculation. $T_m(y)$ is the annual average water temperature at any depth (°C). T_b is the annual average water temperature at the reservoir's bottom. Guangdong belongs to China's south, with a value of 11 °C. T_s is the annual average surface water temperature, and the value is the annual average temperature (20.5 °C), plus the temperature increment (2~4 °C), and the value is 23.5 °C in calculation. H is the depth of the reservoir, (m); $A(y)$ is the annual variation of water temperature, in which the annual variation of surface water temperature A_0 is the same as the annual variation of air temperature, which is 8.57. ε is the temperature phase difference of water.

The surface of the dam is directly in touch with the outer environment, and the heat release coefficient β_{c1} is around 1095.6 kJ/(m^2·d·°C), according to wind speed observation records and reference [29]. The heat release coefficient, β_{c2} is around 400 kJ/(m^2·d·°C) since the substation tunnel's interior is a largely enclosed environment with little surface breeze. The inside of the dam is totally sealed and handled in accordance with the adiabatic boundary, including all corridors, slots, etc.

When calculating the quasi-stable temperature field of the dam, the boundary conditions are: the upstream water level H_w is determined by Equation (15), and the water temperature of each node is determined by Equations (14)–(18). The upstream dam foundation and the portion of the upstream dam face below the water surface are handled in accordance with the first boundary condition. The portion below the water's surface and the foundation of the downstream dam are also handled in accordance with the first boundary requirement. Disturbed by the power plant's tail water, it is assumed that the water temperature downstream is evenly distributed, and the water temperature is taken from the water temperature at the power plant's diversion pipe, with the water level being calculated in accordance with the normal tail water level. The remaining surface of the dam foundation shall be considered an adiabatic boundary. The interior surface of the substation tunnel and the contact surfaces between the dam body and the outside atmosphere are handled in accordance with the third boundary requirement.

When calculating the dam stress field, the boundary conditions are: the surrounding area and bottom of the foundation are supported by connecting rods, and the surface of the foundation and the upper concrete structure are free and unconstrained. The load is imposed as follows: the water level and temperature boundary conditions are constant, and the upstream and downstream portions below the water surface are exposed to water pressure perpendicular to the surface. According to the body load, the structure's self-weight is applied in a vertical downward direction. Since the dam's construction, its temperature field and stress field have been modelled.

Before calculating the temperature field and stress field of the dam, the quasi-stable temperature field of the foundation is calculated by using the multi-year monthly average temperature. Then, the temperature field and stress field of the dam is calculated under the change in multi-year monthly average temperature.

What needs to be clarified is that, in order to increase calculation efficiency, real-time conditions are simplified. For instance, under realistic circumstances, the temperature will change at any time, but we ignore this and instead use the trigonometric function to calculate by fitting the monthly average temperature over a long period of time. This is because the real-time conditions are complex and changeable. If the simulation is carried out completely according to the real-time conditions, the calculation efficiency will not be guaranteed; in addition, it is unnecessary to simulate according to the real-time conditions. Simplifying real-time conditions and calculating with theoretical conditions are common means to calculate the temperature field of mass concrete, such as dams [29,30]. Of course, errors will result from this simplification. For instance, the calculated stress will be lower than the actual stress when the outside temperature is underestimated in the summer.

However, the research demonstrates that there is no discernible impact on the internal temperature field and stress field of mass concrete, regardless of whether the real-time change in the external temperature is taken into account [29]. Since the concrete surface is where the majority of the simplified method's error is concentrated, the concrete surface area's grid has been refined, which somewhat reduces calculation error. The calculated load step is reduced when extreme weather is taken into account, and the sudden outside temperature change is taken into account to as closely mimic the actual situation as possible. Real-time conditions are not taken into account for the normal operation period because the surface concrete's temperature and stress changes are comparatively continuous, which has little bearing on the calculated error value.

3.3. Simulation Cases

In order to investigate the reasons for fractures, the simulation computation primarily considers three scenarios: the temperature field and stress field of the dam under multi-year average temperature (Case 1) and severe weather (Cases 2 and 3).

Case 1 involves determining the overflow dam section's quasi-stable temperature field and accompanying stress field under the impact of the multi-year monthly average temperature during the operational period.

Case 2 is based on Case 1 and takes into account the reservoir's flood discharge condition during a summertime heat wave and thunderstorm; at this period, the dam will experience water cooling shock and water pressure during flood discharge. From 1–10 July, the reservoir's water level maintained its monthly average water level; from 11–20 July, the reservoir's water level increased to the flood limit level without discharging; and from 21–31 July, the reservoir's water level was calculated at 165.53 m. The dam was in a discharge state, and the downstream water level was calculated based on the reservoir's observation data. According to the surface force, the water pressure is applied during water release, and the size is determined by the design data.

On the basis of Case 1, Case 3 replicates the temperature field and stress field of the dam while taking a winter cold wave assault into account. It is decided to use the dam's regular cold wave assault procedure, which involves the cold wave arriving when the temperature is at its lowest point in the year, dropping 10 °C in one day for five days, and then rising to normal temperature in one day.

4. Simulation Result

4.1. Normal Operation Period

Calculations are made of the overflow dam's quasi-stable temperature field and associated stress field under the influence of multi-year monthly average temperatures. The distribution nephograms of the temperature field and stress field in the dam's core section are shown in Figures 4–7, respectively, for the months of April, July, October, and January. It should be noted that the stress nephogram in this paper is the first principal stress, which means that the tensile stress mentioned in this paper is the principal stress.

The temperature nephogram demonstrates that the concrete in the region below the upstream water level is primarily influenced by the water temperature, resulting in a low temperature and a small temperature change. The concrete in the area above the upstream water level, the overflow dam surface, and the area near the substation tunnel are easily affected by the outside temperature change. The temperature of the overflow surface is high in summer, reaching 30 °C. In winter, the temperature of the overflow surface is low, only 12 °C, and the temperature varies greatly every year. The temperature calculation result is consistent with the research conclusion of Mingchao Li et al. [31].

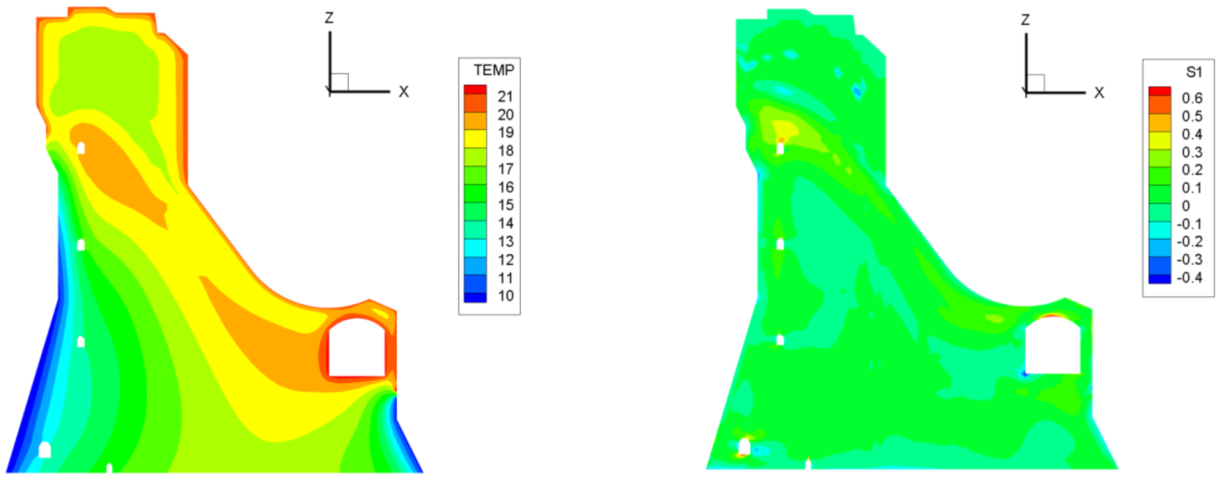

(**a**) (**b**)

Figure 4. April of normal operation period. (**a**) Temperature field (°C), (**b**) Stress field (MPa).

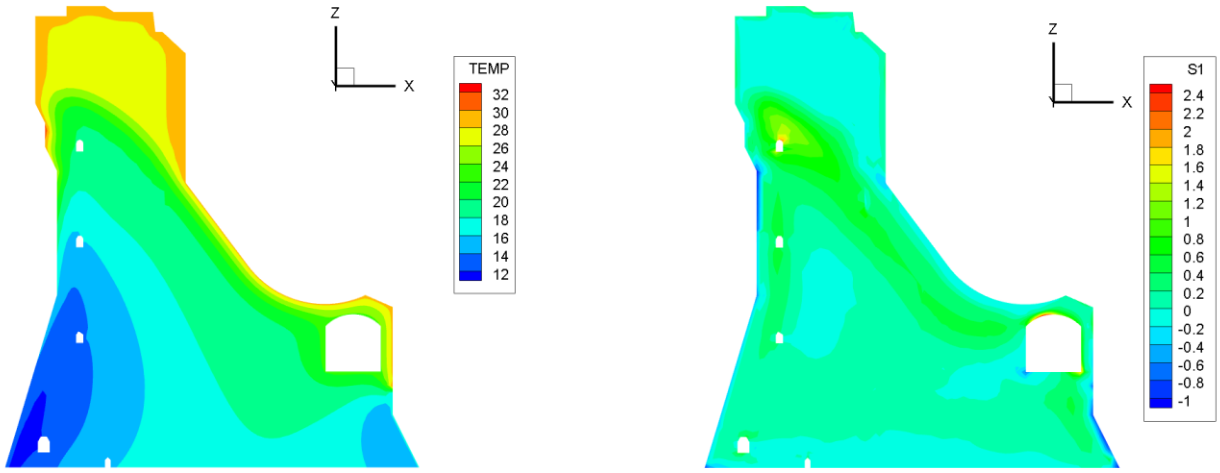

(**a**) (**b**)

Figure 5. July of normal operation period. (**a**) Temperature field (°C), (**b**) Stress field (MPa).

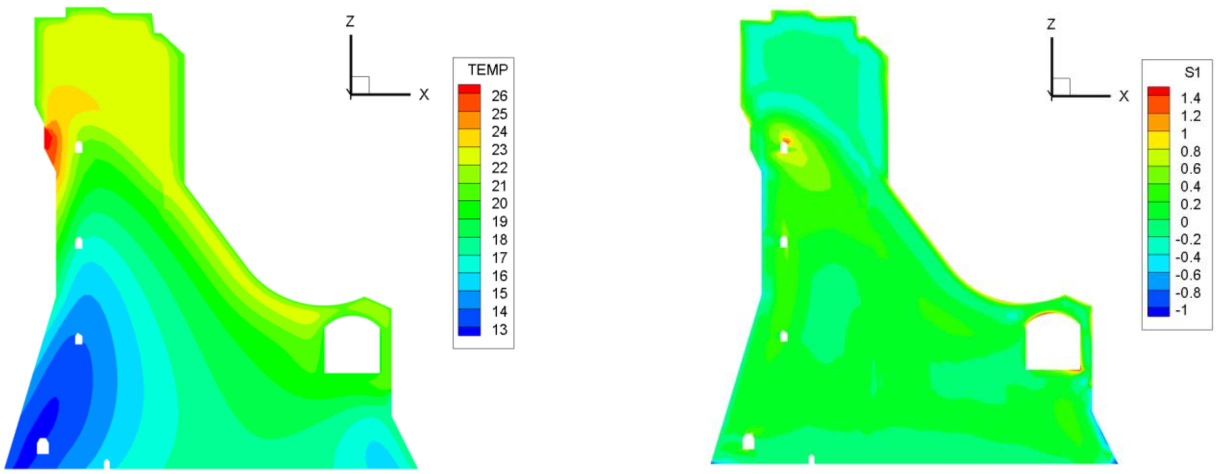

(**a**) (**b**)

Figure 6. October of normal operation period. (**a**) Temperature field (°C), (**b**) Stress field (MPa).

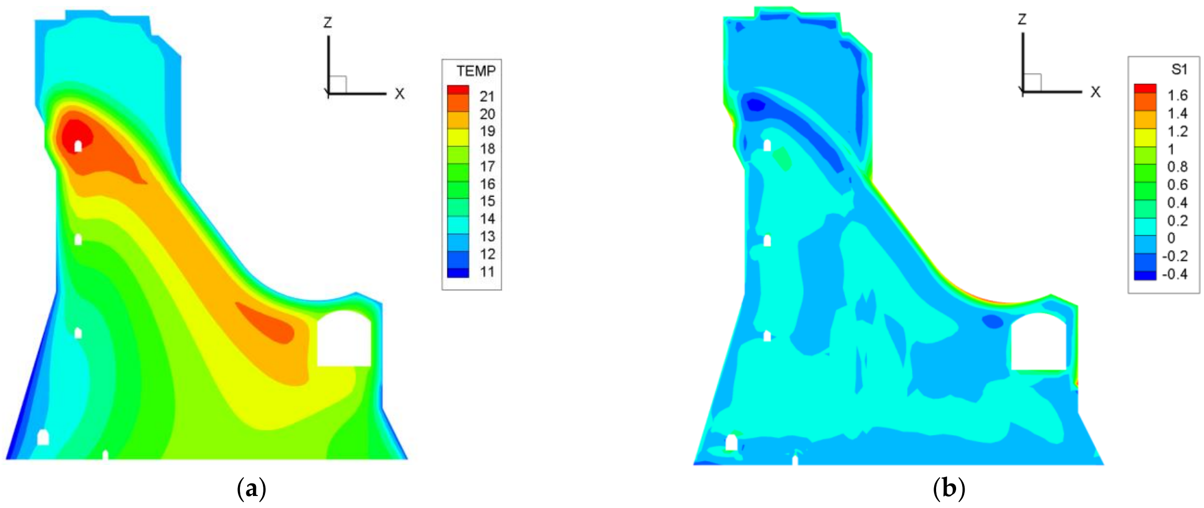

Figure 7. January of normal operation period. (**a**) Temperature field (°C), (**b**) Stress field (MPa).

Among them, in October (Figure 6a), the temperature of the concrete near the upstream water level was significantly higher than that of the surrounding concrete, which is explained as follows: In summer, the temperature of the concrete in the surface area near the water surface is high, and the heat is gradually transferred to the dam with the passage of time. As time goes by, when the temperature of the surface area decreases, the heat stored inside will radiate to the surface, so the temperature of this part of the area is higher than the air temperature. At the same time, the temperature of the concrete below the water surface is relatively low due to the temperature of the reservoir water. When the height of the concrete in the above part exceeds 158.4 m, the temperature is relatively low because the structural thickness is reduced, and the heat stored inside is easier to dissipate. When the height of the concrete above the water surface exceeds 158.4 m, the temperature of the concrete is relatively low because the thickness of the structure is reduced, and the heat stored inside is easier to dissipate. At the same time, the temperature of the concrete below the water surface is relatively low due to the temperature of the reservoir water.

The stress nephogram shows that in April, the overflow dam section's total stress was low—all values were below 0.6 MPa—and the structure was safe. The inner portion to the left of the top of the substation tunnel has a tensile stress of 2.4 MPa in July, which is higher than the tensile strength of concrete (1.5 MPa). The dam safety inspection findings, which are in line with the estimated findings, indicate that the concrete in this location has significant fissures. In the fall of October, it was noted that the tensile stress was relatively high, reaching 1.4 MPa but not exceeding the tensile strength at the top of the substation tunnel, the thin wall on the right side, the corner on the lower right side, and the area near the anti-arc section of the overflow surface. The overflow surface's anti-arc portion experiences high tensile stress in January of each year, reaching 1.6 MPa, making the structure unstable and prone to fractures. The calculated results of stress are close to those of Léger, P. et al. [32], and Bofang Zhu's [29] research result.

Two distinguishing points are chosen in the center of the overflow dam section for observation in order to further investigate the causes of fractures in the anti-arc portion of the overflow surface and the top of the left side of the substation tunnel. As depicted in Figure 8, the characteristic Point 1 is where cracks appear at the top of the substation tunnel, and the characteristic Point 2 is where cracks appear in the reverse arc section of the overflow surface. As illustrated in Figure 9, the temperature and stress duration curves are retrieved. The graphic shows that the temperature and stress trends at key point 1, which is at the top of the substation tunnel, are similar, and that the tensile stress rises as the temperature rises. Its location in the substation tunnel results in a slight temperature change but a huge variation in stress, with a peak tensile stress that even surpasses the tensile strength at 2.64 MPa. It can be observed that the simulated and observed fractures are in the same location in Figure 10, which depicts the cracks that were really seen at the top of the substation tunnel in the overflow dam portion.

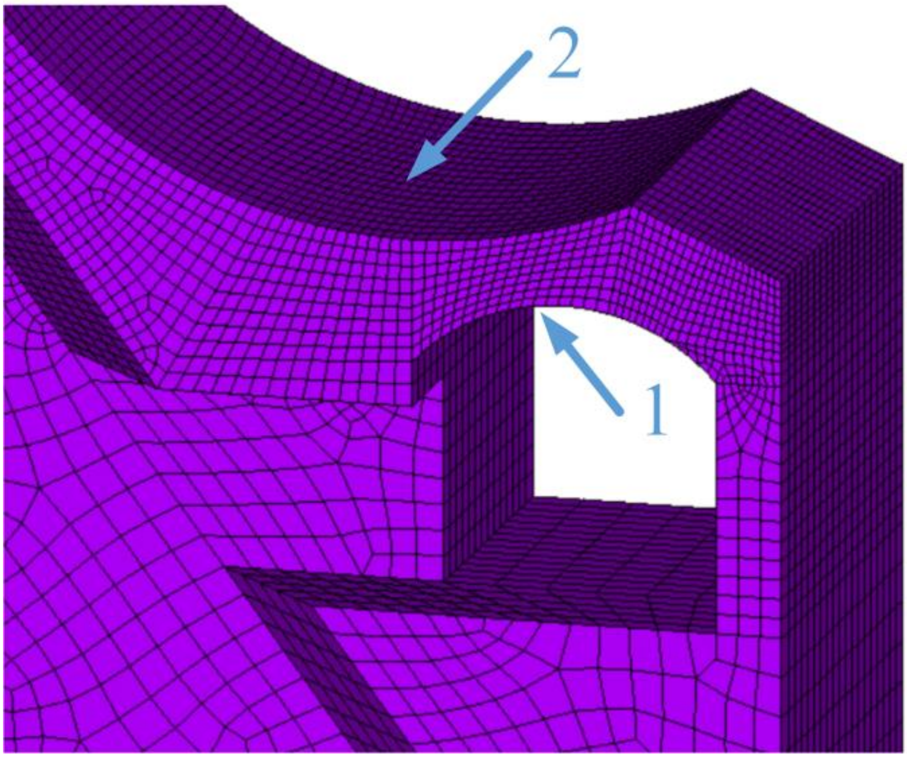

Figure 8. Schematic diagram of key point positions.

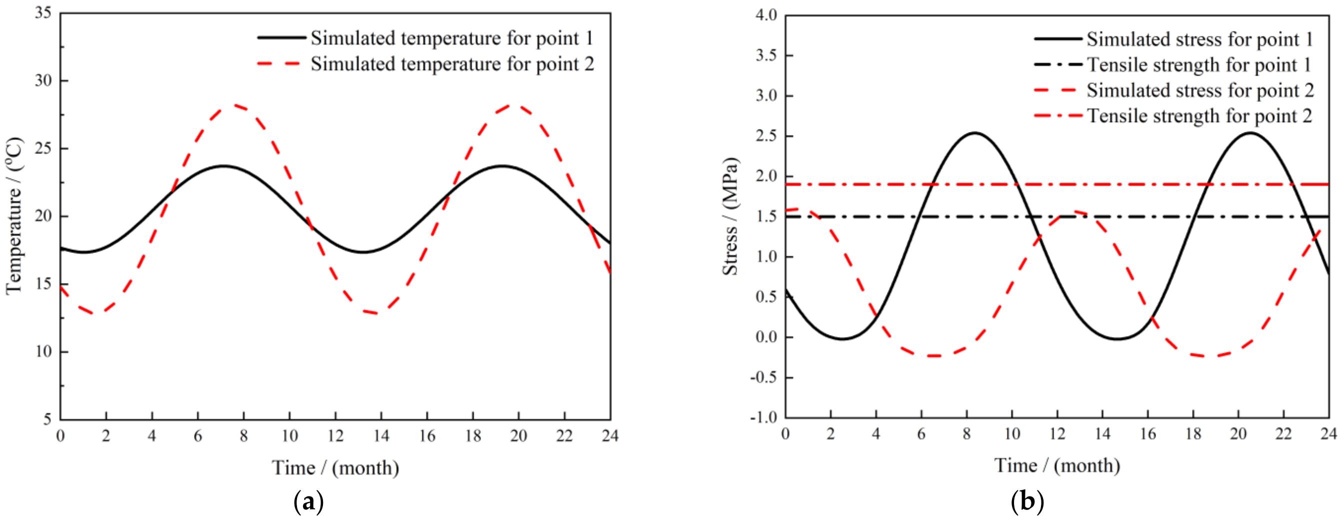

Figure 9. Duration curve of key points. (**a**) Temperature (°C), (**b**) Stress (MPa).

As observed in Figure 9, the temperature at Key Point 2 in the anti-arc section declines as the tensile stress rises, which is the reverse of the ambient temperature. The temperature changes considerably because of the atmosphere's direct interaction. In addition, when the temperature drops in winter, the concrete on the overflow surface contracts owing to the drop in temperature, increasing the tensile stress. Tensile stress peaked at 1.62 MPa; while it fell short of the tensile strength (1.9 MPa), it was nonetheless harmful.

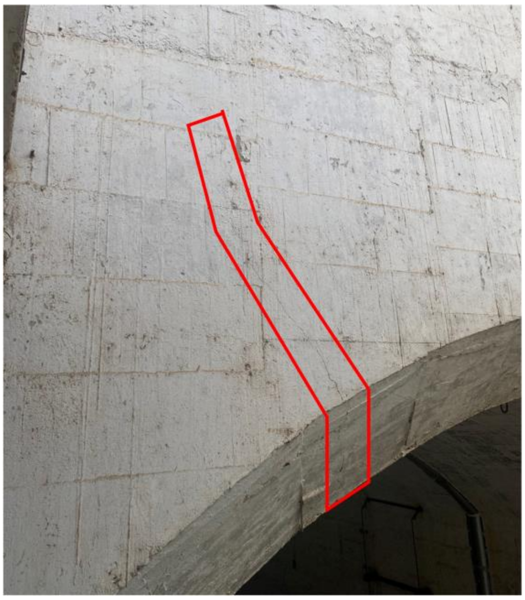

Figure 10. Observation cracks at the top of the substation tunnel.

4.2. Cause Analysis of the Crack at the Top of Substation Tunnel

The reasons for concrete tensile stress in the left section at the top of the substation tunnel will be examined in the paragraphs that follow. The temperature and stress field and temperature nephogram near the substation tunnel in July are shown in Figure 11. It is evident that in the summer, the temperature near the overflow surface is high and the temperature within the substation tunnel is quite low; the difference in temperature is around 4–5 °C. The structure is vulnerable to cracking due to the high tensile stress at the corner at the lower right and the left section at the top of the substation tunnel. In other places, the tensile stress is just 1.2 MPa or less, which is an acceptable amount.

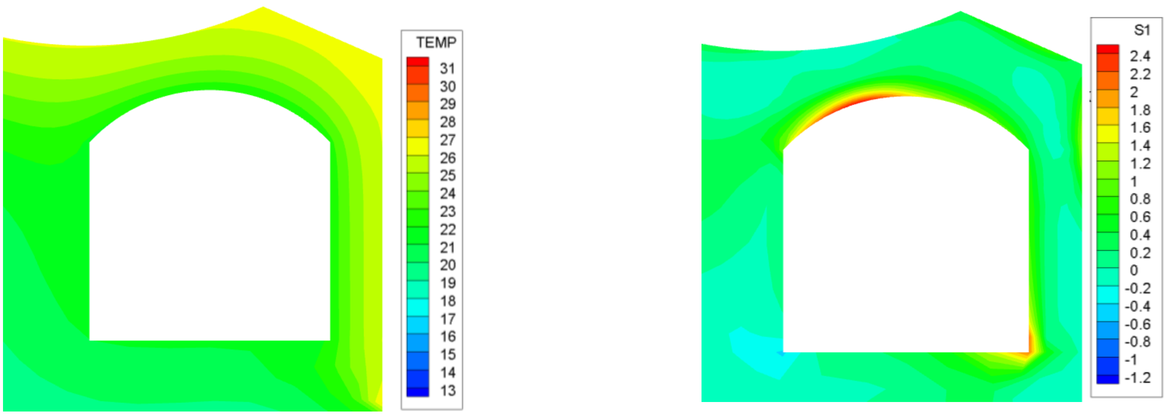

(**a**) (**b**)

Figure 11. Simulation results near the substation tunnel at the moment of maximum stress. (**a**) Temperature field (°C), (**b**) Stress field (MPa).

The total deformation in ANSYS refers to the displacement of the structure under the load. Therefore, the total displacement u of nodes in the area near the substation tunnel at the moment of maximum stress can be extracted ($u = \sqrt{u_x^2 + u_y^2 + u_z^2}$, u_x, u_y, u_z are displacement in three directions), and the total deformation of the structure under the load can be obtained, as shown in Figure 12. The dotted line in the figure shows the original outline of the dam, and the solid line shows the deformation outline of the dam under the load (magnified by 800 times). As can be observed, the thin wall next to the substation tunnel exhibits significant deformation in the summer owing to the effects of temperature, particularly at the top and right side. This is because the heated and expanded concrete in the upper portion of the substation tunnel's top causes the downstream thin-walled wall to bend to the right, increasing the tension at the tunnel's right lower-side turning point. The thin-walled wall is heated and extended, which causes the top portion of the substation tunnel to flex upward and stretch the lower portion on the left side of the top portion. Simultaneously, the concrete in the substation tunnel's top is heated and expanded, which causes it to move to the right and create tensile stress on the concrete on the bottom side of the top.

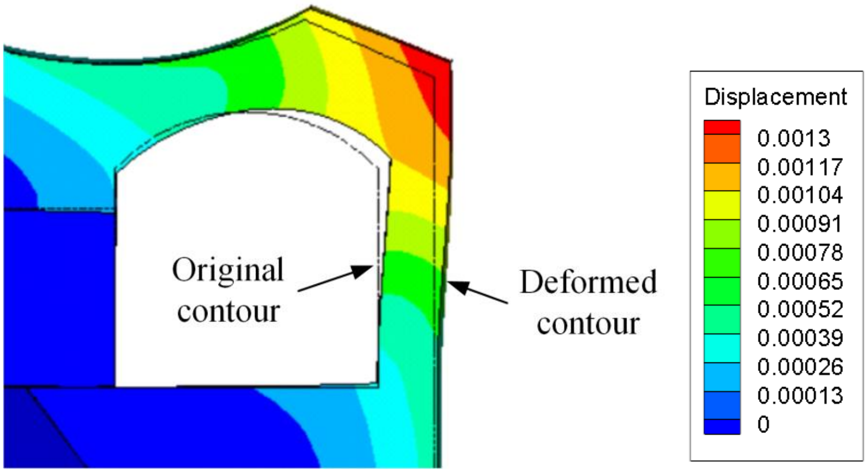

Figure 12. Total deformation near the substation tunnel in July (deformation enlarge 800 times, unit m).

It is clear from the temperature and stress duration curves in Figure 9 that there is a strong correlation between the stress change at Point 1 and the yearly temperature change, leading one to hypothesize that the temperature change is the primary source of the tensile stress. The material's linear expansion coefficient was altered in order to do more research on the sources of tensile stress. Equation (7) states that the temperature load is delivered as a body load and that the linear expansion coefficient significantly affects the temperature load. In order to examine the impact of various factors on the tensile stress in the left area at the top of the substation tunnel, the linear expansion coefficient of the concrete close to the substation tunnel is reduced to 1/100 of the original value, rendering it incapable of thermal expansion and cold contraction.

The concrete's linear expansion coefficient is decreased in the thin wall section on the right side of the substation tunnel, as illustrated in Figure 13a (red region). The temperature field findings are unaffected because only the linear expansion coefficient is altered, and the stress nephogram of the dam in July (Figure 13b) and the stress duration curve at Point 1 (Figure 14) are as a consequence. When comparing Figures 11b and 13b, it can be seen that the distribution of tensile stress has not changed significantly, but the peak value has dropped from 2.65 MPa to 2.32 MPa, a drop of 0.33 MPa and a reduction of 12.45%. It demonstrates that, although it has a little impact, the right side's thin wall will expand upward in response to summer's high temperatures, elevating the concrete at the top of the substation tunnel and dragging the left area.

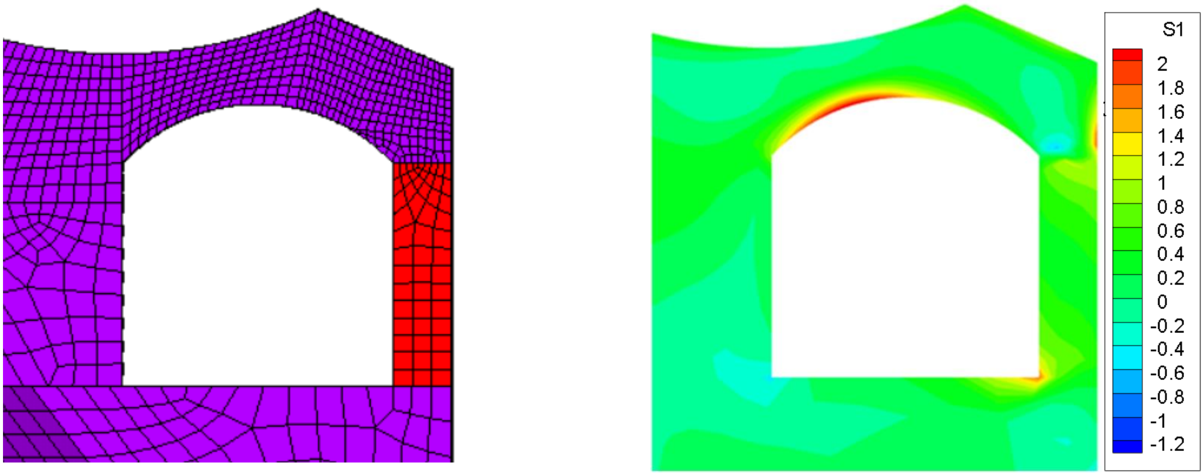

(**a**) (**b**)

Figure 13. Calculation scheme 1 (**a**) Change the coefficient (red area), (**b**) Stress field (MPa).

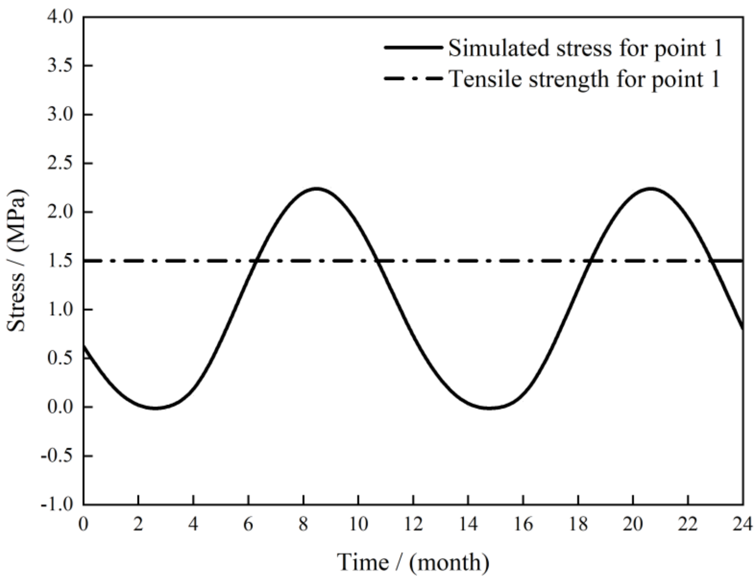

Figure 14. Stress duration curve of Point 1 under calculation scheme 1.

The thin-wall portion on the right side of the substation tunnel and the concrete on the right side of the top of the substation tunnel (red region) both have a lower linear expansion coefficient, as illustrated in Figure 15. Both the stress duration curve of Point 1 (Figure 16) and the stress nephogram of the dam in July are obtained. Tensile stress is now still over the tensile strength (1.5 MPa) at the left region at the top of the substation tunnel and is still very high. Tensile stress' peak value, on the other hand, dropped from 2.32 MPa to 1.67 MPa and by 0.65 MPa, a reduction of 24.5%. Inference: The concrete in the right region at the top of the substation tunnel will expand when heated in the summer, forcing the concrete in the left section to migrate higher and become strained.

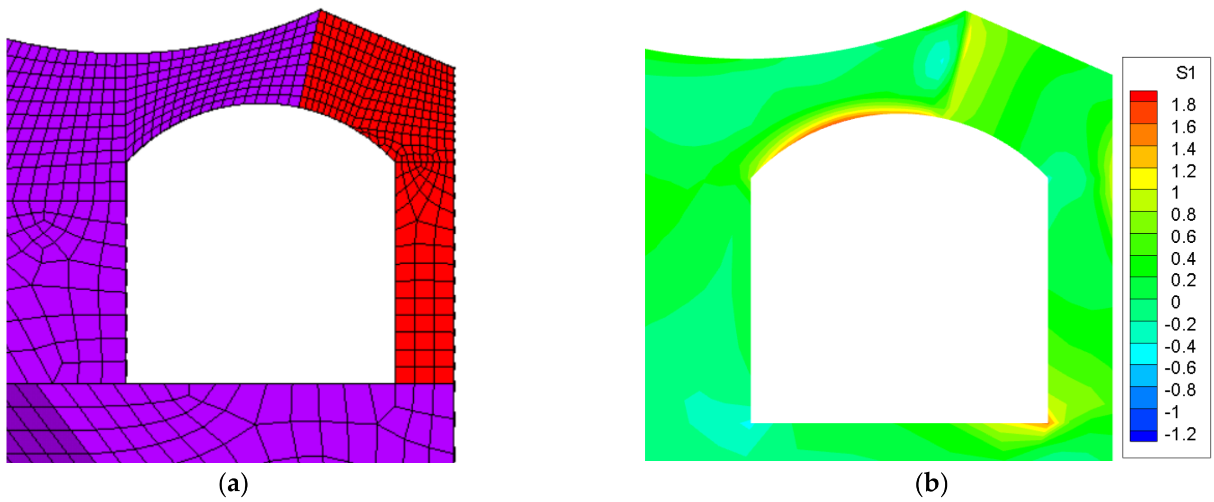

Figure 15. Calculation scheme 2. (**a**) Change the coefficient (red area), (**b**) Stress field (MPa).

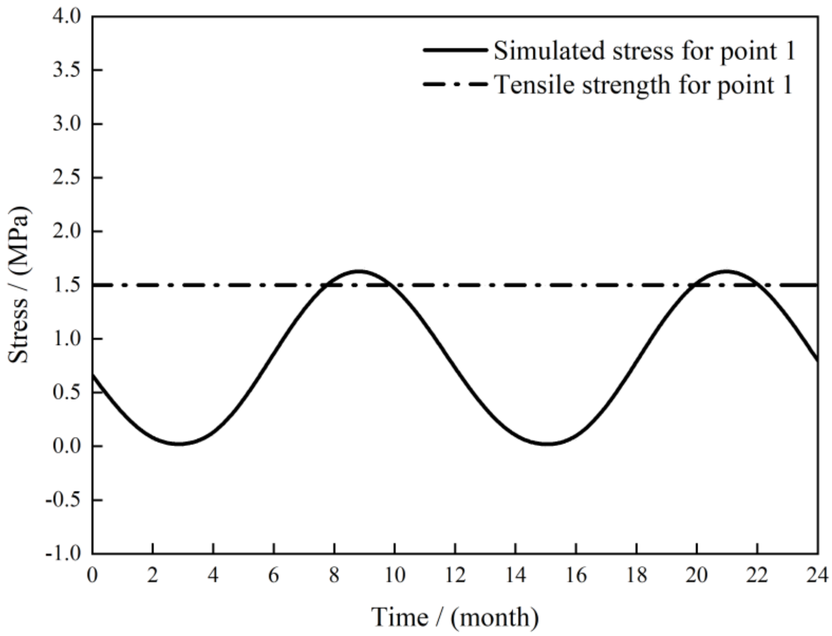

Figure 16. Stress duration curve of Point 1 under calculation scheme 2.

The thin-wall portion on the right side of the substation tunnel, the right region at the top of the substation tunnel, and the surface area of the overflow dam (red area) all have lower linear expansion coefficients of concrete, as illustrated in Figure 17. Both the stress duration curve of Point 1 (Figure 18) and the stress nephogram of the dam in July are obtained. The tensile tension will now start to decrease once again in the left section near the top of the substation tunnel. Tensile stress' peak value dropped from 1.67 MPa to 0.67 MPa, a drop of 1 MPa and a reduction of 37.7%. It can be assumed that the concrete in the surface area of the overflow dam will pull and displace the concrete in the lower area of the corresponding substation tunnel to the right, increasing the tensile stress, and that the concrete in the upper area of the top of the substation tunnel will also be pushed to the right when heated and expanded in the summer.

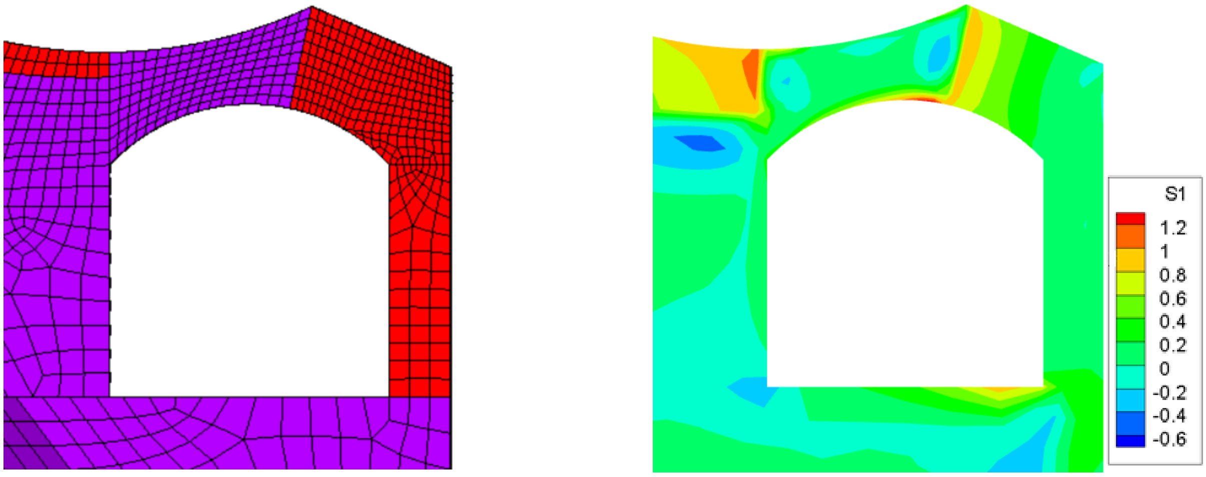

(a) (b)

Figure 17. Calculation scheme 3. (**a**) Change the coefficient (red area), (**b**) Stress field (MPa).

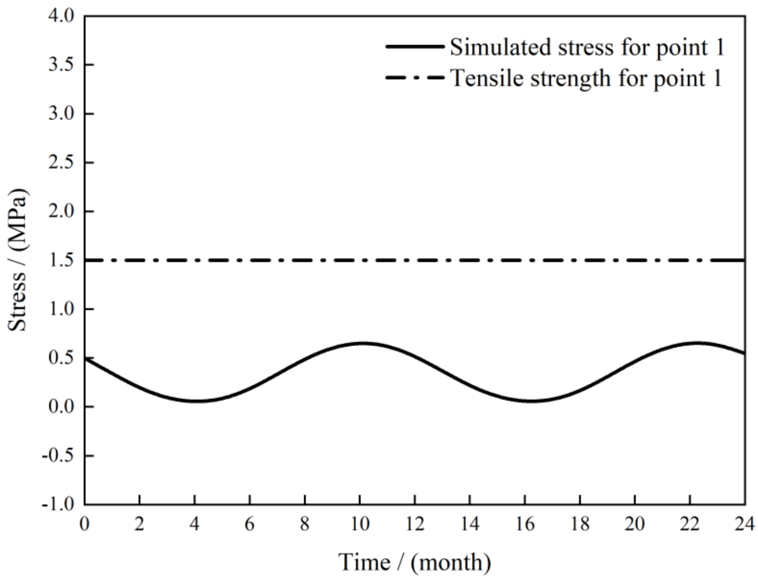

Figure 18. Stress duration curve of Point 1 under calculation scheme 3.

4.3. Influence of Extreme Weather

Figure 19 shows the nephogram of the temperature field and stress field during Case 2's central overflow dam discharge. The temperature nephogram demonstrates how water discharge will cause the overflow dam's surface temperature to drop. The tensile stress of the concrete in the left section near the top of the substation tunnel is still significant, as can be seen from the stress nephogram. The temperature of concrete within the substation tunnel has no visible change during water discharge, and the peak value is still 24 °C, as can be seen from the temperature and stress duration curve of Key Point 1 in Figure 20. The peak stress will nonetheless rise a further 0.28 MPa to 2.93 MPa. This is due to the fact that the top of the substation tunnel will be equal to the beam structure under the influence of water pressure, and the concrete in the lower region will be under tension, increasing the tensile stress and making fractures more likely to appear.

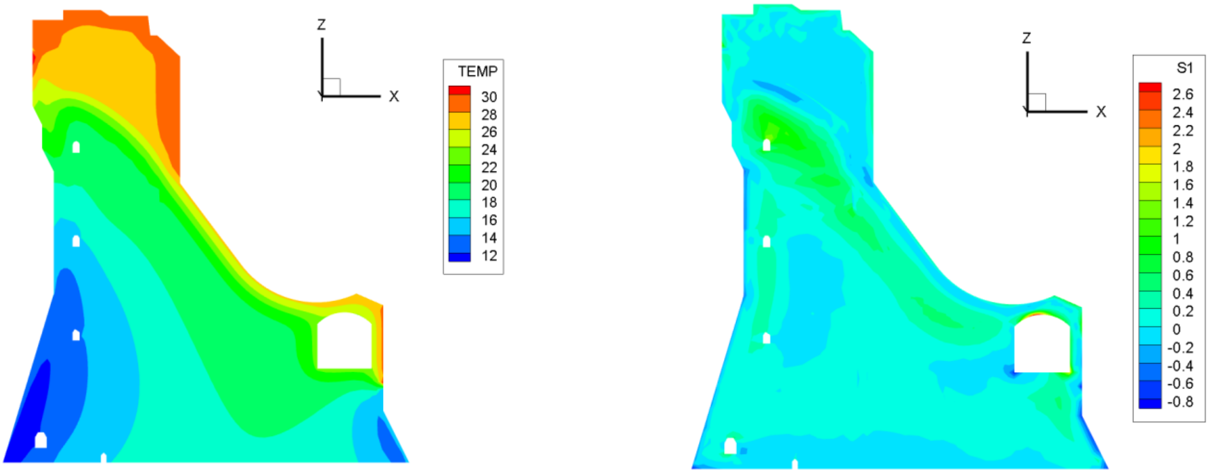

(**a**) (**b**)

Figure 19. High temperature and water discharge in summer. (**a**) Temperature field (°C), (**b**) Stress field (MPa).

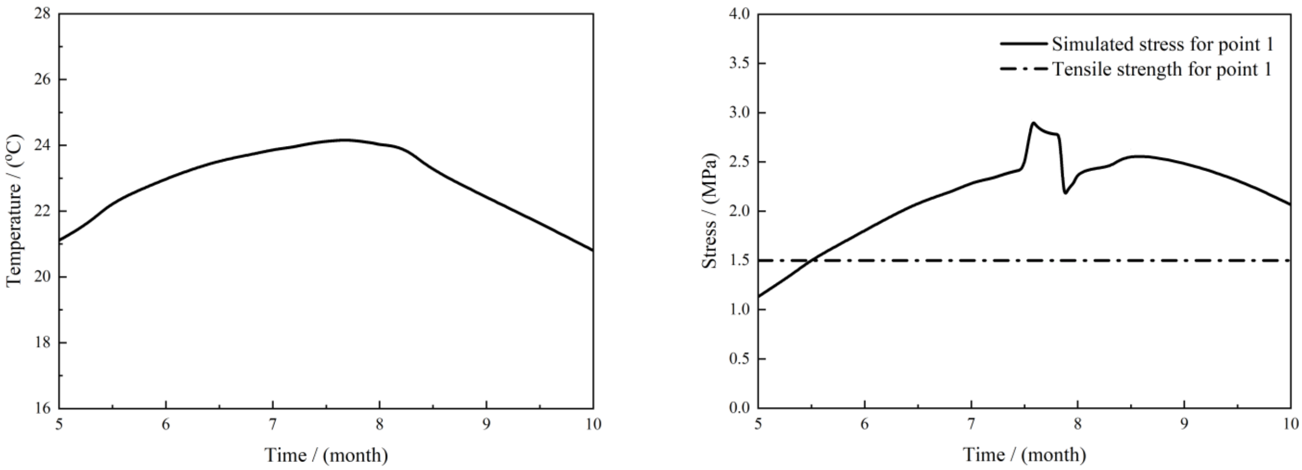

(**a**) (**b**)

Figure 20. Duration curve of Key Point 1 under Case 2. (**a**) Temperature (°C), (**b**) Stress (MPa).

The major reasons for the deep cracks that have developed in the inner region on the left side of the substation tunnel's top may be determined using the study from Section 4.2. Summertime temperature increases cause the concrete on the dam surface to heat up and expand, as well as the thin right wall of the substation tunnel, the top right section, and the overflow dam surface. Compared to the surface concrete that is in direct contact with the atmosphere, the temperature of the concrete in the left area at the top of the substation tunnel will also rise because it is in a relatively enclosed space. However, the temperature is relatively low, and the expansion trend is relatively small. The concrete at the bottom of the substation tunnel will create roughly 1 MPa of pressure due to the deformation brought on by the temperature increase as the higher concrete pulls the lower concrete to expand to the right. Concurrently, the concrete on the substation tunnel's right side will be heated and expanded, which will cause the concrete on the tunnel's left side to move upward. Currently, a tensile stress of 0.98 MPa is produced. A 0.67 MPa tensile stress will also be produced by the concrete in this location due to its own weight, as well as the impact of its own temperature load. The tensile stress of the concrete in this location will be larger, reaching 2.65 MPa, surpassing the tensile strength (1.5 MPa), and leading to fractures under the combined impact of these forces. This beam construction will have an increase in tensile stress due to the influence of water pressure of around 0.30 MPa, which will be added to the thermal stress and be close to 3 MPa, which is more likely to result in fractures.

The temperature field and stress field when a cold wave hits the middle part of the overflow dam under Case 3 are shown in Figure 21. As indicated in Figure 21a, when the cold wave hits, the overflow dam's surface temperature will drop to roughly 3 °C. The anti-arc region of the overflow surface will experience a strong rise in tensile stress at this point, reaching around 4 MPa (red dotted line area), as can be shown in Figure 21b. The concrete temperature in the overflow area will drop by about 10 °C when the cold wave hits, and the stress will rise sharply by about 2.4 MPa, reaching 4 MPa, exceeding the tensile strength (1.9 MPa), according to the temperature and stress duration curve of Key Point 2 in Figure 22. The distribution pattern of the discovered anti-arc section fractures is shown in Figure 23. It is discovered that this region has connection cracks, and the placement of the cracks is compatible with the findings of the calculations.

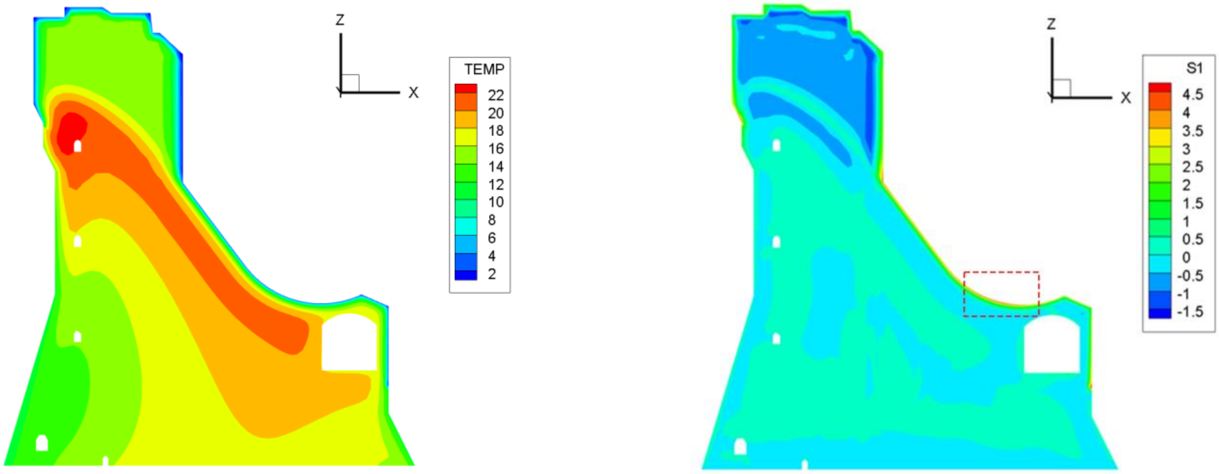

(**a**) (**b**)

Figure 21. Cold wave attack in the winter. (**a**) Temperature field (°C), (**b**) Stress field (MPa).

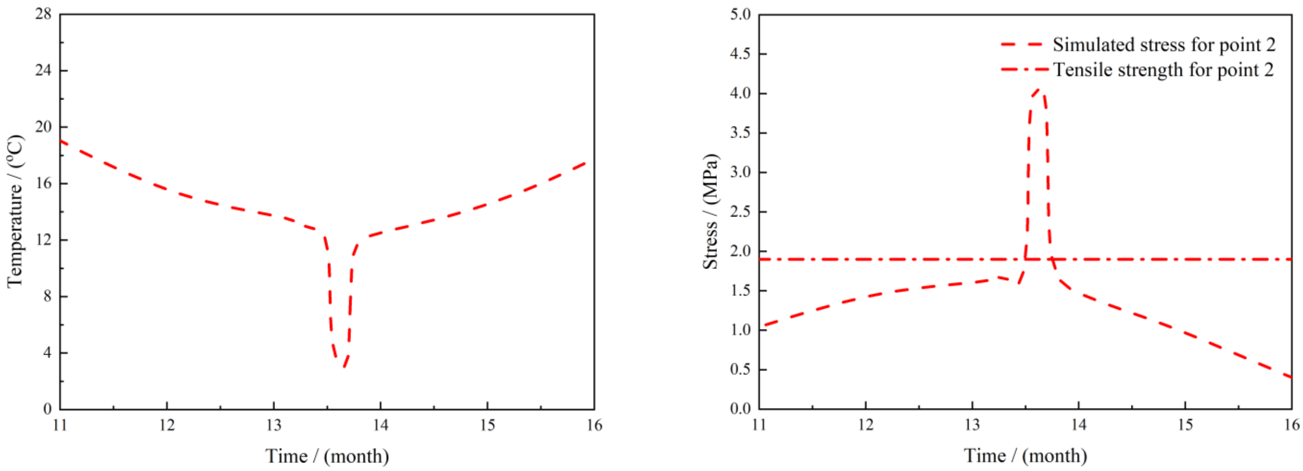

(**a**) (**b**)

Figure 22. Duration curve of Key Point 2 under Case 3. (**a**) Temperature (°C), (**b**) Stress (MPa).

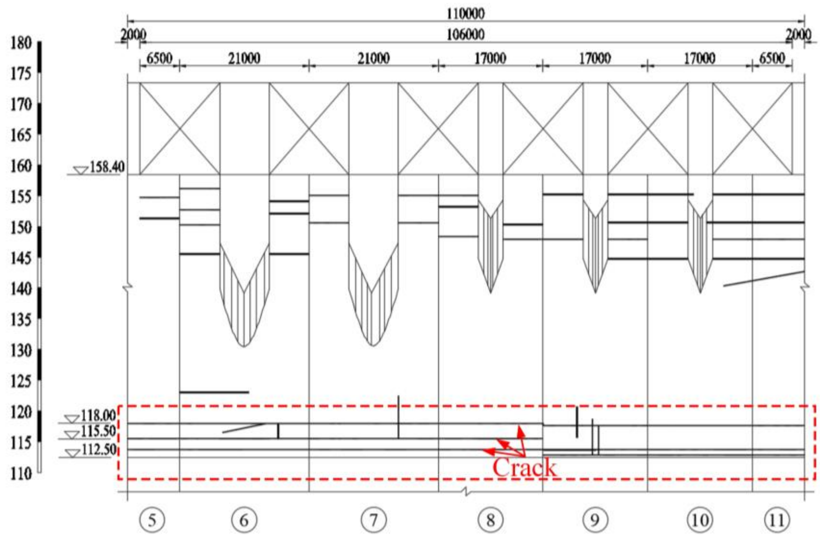

Figure 23. Schematic diagram of crack distribution in an anti-arc section (downstream elevation view. The number in the Figure, like ⑤, represents the dam section).

Consequently, the cause of the anti-arc section's connected surface cracking can be identified. The surface produces a significant tensile stress of roughly 1.6 MPa as the temperature lowers in the winter because the surface area contracts owing to the cold while being constrained by the lower concrete. The overflow dam's surface area experiences significant cooling and a fast decrease in temperature when the winter cold wave (10 °C below usual wintertime temperatures) arrives. As a result, the concrete on the overflow dam's surface contracts even more. Horizontal fractures occur when the tensile stress exceeds the tensile strength (1.9 MPa) by 4 MPa.

4.4. Compared with the Monitoring Results

In January 2017, two crack gauges (J05–J06) were placed at the left and right guide walls of the anti-arc portion of the overflow surface, and four crack gauges (J01–J04) were set at the horizontal cracks at the top of the substation tunnel to monitor the major cracks. Figures 24 and 25 depict the correlation diagram between the crack gauge monitoring data and the water and air temperatures.

The crack gauges J01–J04 are not in direct contact with the atmosphere, which is equal to the interior environment, since they are located at the horizontal cracks at the top of the substation tunnel. Therefore, the variations in temperature are not readily apparent. The opening and closing degrees of the J01 and J03 monitoring points are largest in July and smallest in January, which is consistent with the calculation results of Case 1 and indicates that the concrete in the left area at the top of the substation tunnel will be removed in July. It is difficult to see how the crack opening has changed at the J02 monitoring site. While the amplitude is small, the change trend at the J04 monitoring point is similar to that at the J03 point.

The crack opening clearly varies with temperature since the crack gauges J05 and J06 are positioned on the overflow dam's surface and in touch with the environment. The crack hole shrinks and tends to shut as the temperature increases. On the other hand, when the temperature lowers and the split opens wider, it tends to be dragged open. The measured gauge measurement value and temperature have a negative association, which is consistent with the Case 1 computation result. In other words, as the temperature drops, the concrete on the anti-arc section's surface contracts and experiences tensile stress. Cracks will appear when the tensile stress is greater than the tensile strength of the concrete.

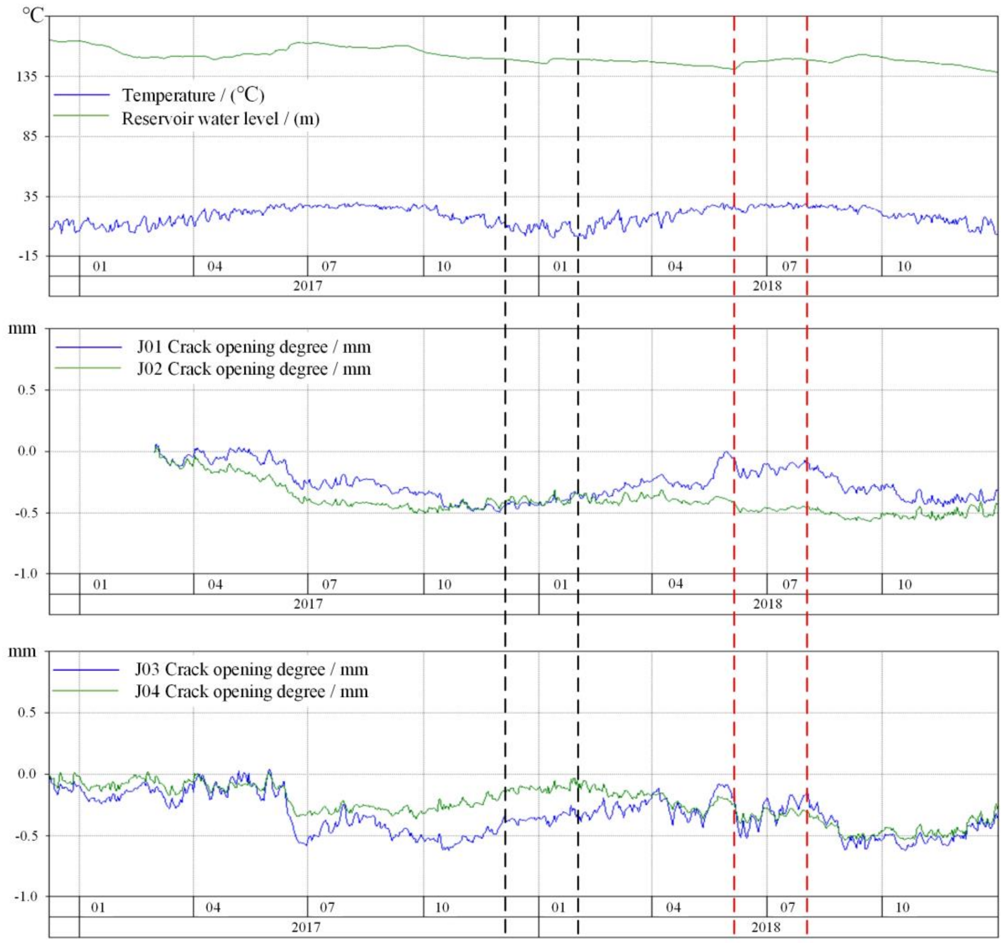

Figure 24. Correlation between the crack opening at the top of the substation tunnel and atmospheric temperature.

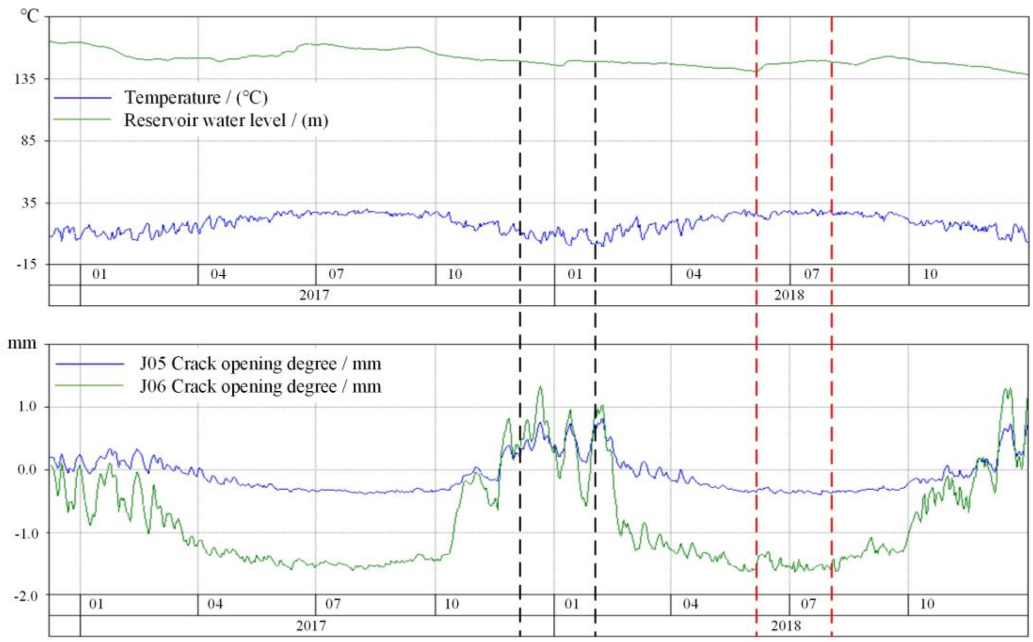

Figure 25. Correlation between the crack opening in anti-arc section of overflow surface and atmospheric temperature.

5. Discussion

The anti-arc section of a gravity dam's overflow surface and the cracks at the top of the substation tunnel are both examined in Section 4 for their root causes. It has been determined that cracks are primarily caused by thermal stress. The fundamental condition is, on the one hand, the expansion or contraction of concrete due to temperature changes. On the other hand, the internal source of excessive thermal stress is the fully constrained substation tunnel structure. These cracks caused by excessive thermal stress during operation can be avoided in the design stage.

Reasonable structural cracks may be included into the design to lessen the structural limitations and prevent excessive thermal stress if the same overflow powerhouse shape as the hydropower station is still utilized. The basic construction of the overflow powerhouse of the Xin'anjiang Hydropower Station in Zhejiang Province, China, is seen in Figure 26. This powerhouse was the subject of this paper's study. The distinction is that it uses structural fissures and expansion plates to connect the dam body and powerplant. As a result, it is evident that the structural limitations are lowered. In addition, high heat stress is avoided. No apparent fractures have been discovered in the anti-arc portion of the powerhouse and overflow surface since the hydropower plant was placed into service in 1960, demonstrating the logic of this treatment strategy.

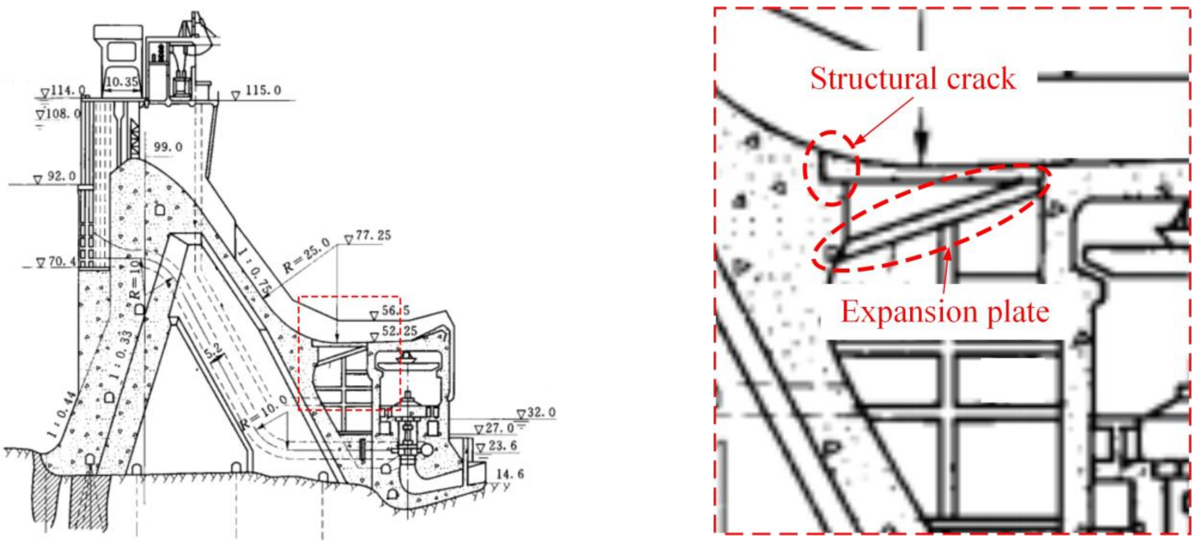

(a) (b)

Figure 26. Xin'anjiang Hydropower Station Profile. (**a**) Overall structure diagram, (**b**) Partial enlarged detail.

The emergence of fractures compromises the structure's structural integrity, and internal steel bars may speed up corrosion after losing their protective coating of concrete, which has a significant impact on the structure's safety. Therefore, it is essential to address this issue. There are primarily two distinct repair strategies at this point. In the first kind, the damaged concrete is scraped away and replaced with fresh concrete that is stronger. The second method simply fixes the cracks while keeping the original concrete and strengthening it with anchor rods or steel plates.

The concrete on the left side of the top of the substation tunnel is totally removed, and new concrete with greater strength is poured in its place, as shown in Figure 27. This is a typical first-class restoration design. The benefit of this plan is that it can be guaranteed that the tensile stress of freshly poured concrete will not exceed the tensile strength in various situations after applying suitable temperature control measures, such as lowering the pouring temperature and the adiabatic temperature increase of concrete. However, due to the drawbacks of difficult construction, the destruction of the original structure, and the high cost, it is not advised.

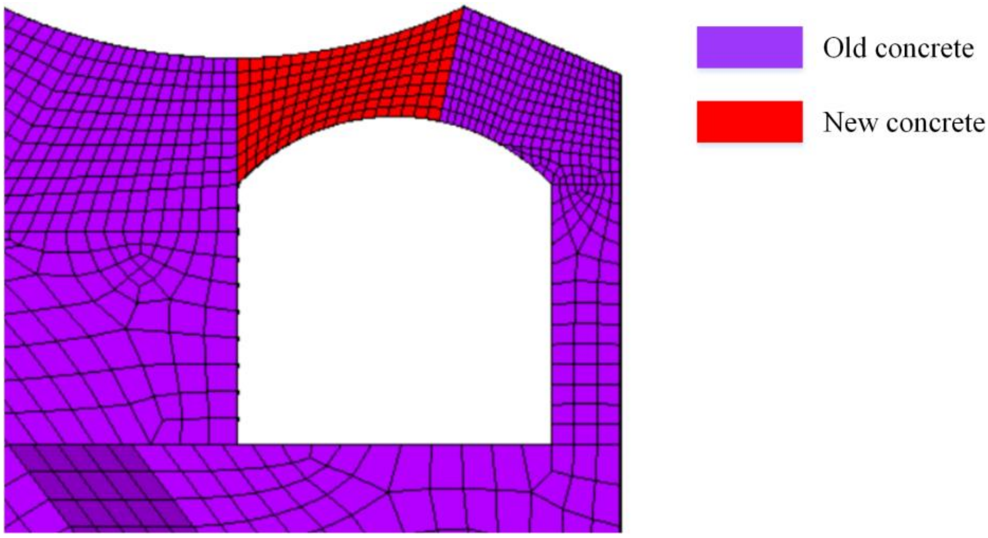

Figure 27. Repair Scheme 1.

A row of anchor rods is hammered into the top of the substation tunnel in Figure 28's typical second repair design, and the figure also shows their locations. The Grade IV fine-rolled threaded steel bar 40Si2MnV, which has a diameter of 32 mm and a length of 20 m, is chosen as the anchor based on the results of the calculations. The steel bars are spaced 300 mm apart, the same as the distance between the steel bars that were first established. In order to ensure the dam's safe functioning under various conditions, the existing fractures are simply fixed. This plan may fully use the steel bars' ability to restrict fracture growth and stop it from spreading. However, because the anchor rod must pass through three layers of steel mesh, which could harm the original structure, it is challenging to ensure that the original steel bar is not harmed.

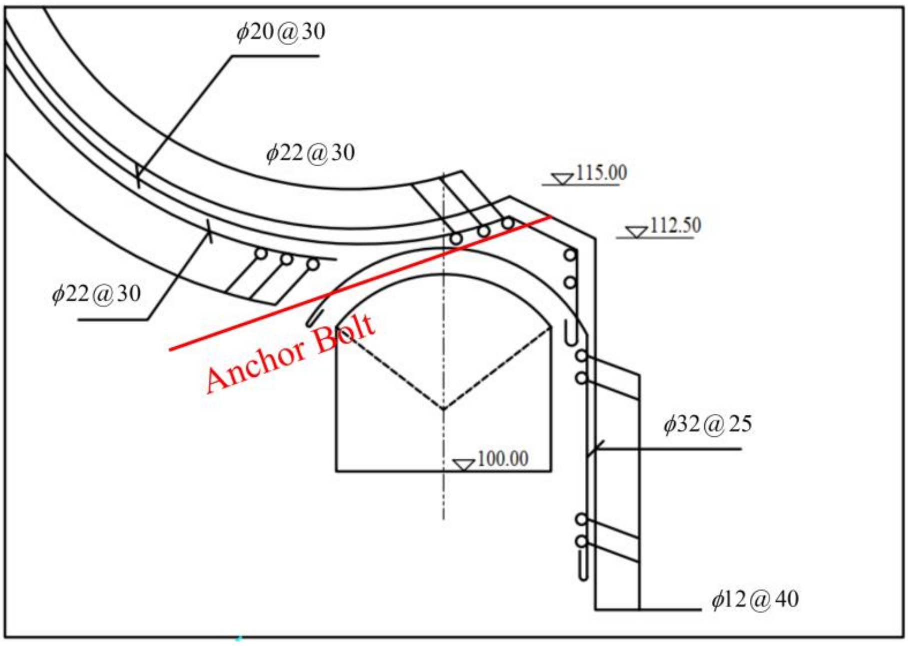

Figure 28. Repair Scheme 2. (ϕ represents rebar diameter, @ represents the spacing between rebar).

The second sort of repair strategy is shown in Figure 29. In order to stop the corrosion of steel bars and structural leaks, first, the local fractured concrete where the deep cracks are found is removed. Next, inorganic binding materials are employed for grouting and backfilling. After that, a steel plate with a 10-mm thickness was erected on top of the substation tunnel, and high-strength structural glue was utilized to join the steel plate to the old concrete. A 0.5 m-deep anchor rod was also driven at the same time to secure the steel plate to the building. To stop leaks, steel plates are joined together by welding, and corrosion protection is applied to the surface. This technique can assure the safe functioning of the dam under various conditions and is simple to build with little harm to the existing construction. The suggested repair plan is this:

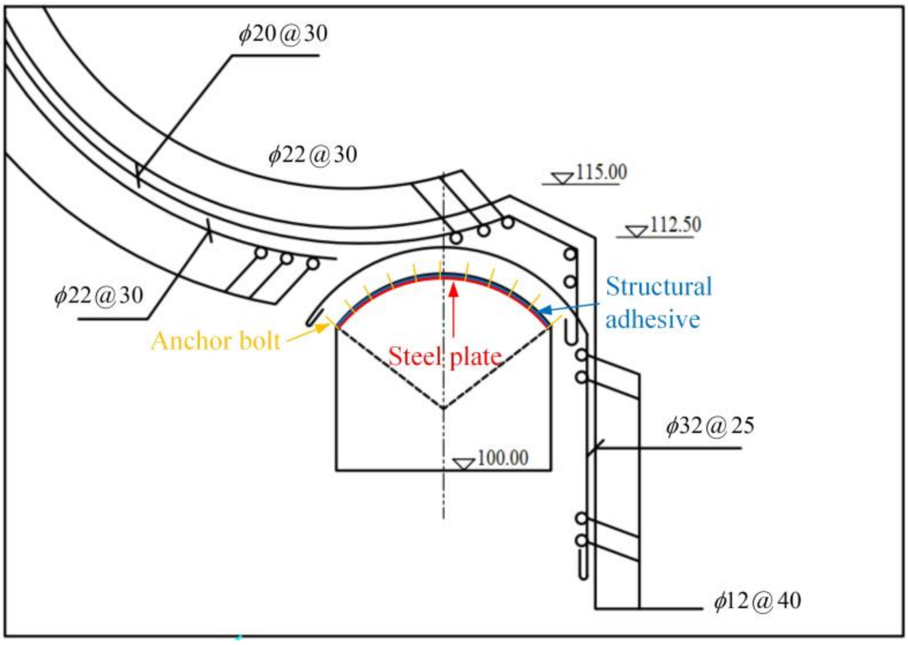

Figure 29. Repair Scheme 3 (ϕ represents rebar diameter, @ represents the spacing between rebar).

It is necessary to remove the damaged concrete, use inorganic binding materials for grouting and backfilling to prevent the steel bars from rusting, ensure water stopping, and conduct long-term crack monitoring if the cracks in the anti-arc section of the overflow dam spread to the surface of the steel bars. If the fracture is small, all that is required to keep water from seeping into the substation tunnel and threatening the equipment's safety is to stop it on the surface.

It is challenging to simulate the construction period of the concrete gravity dam under study in this paper because it has a long history, and some construction data are missing. As a result, the initial thermal stress brought on by the concrete's hydration heat is not taken into account in the simulation. In later research and mass concrete building design, we can simulate the structure's temperature and stress during the construction period and carefully take into account various cases during the operation period, in order to prevent the occurrence of temperature cracks as far away from the root as possible and ensure the structure's safe operation. Additionally, the calculation ignores the impact of internal reinforcement, which can be improved in the subsequent study by making use of the analysis of pertinent literature [33].

In this paper, only the overflow powerhouse in gravity dams is discussed and analyzed in depth, and the analysis of other types of gravity dams is limited. In the underground factory building structure with relatively constant temperatures, this type of temperature cracks caused by the rigid constraints, unreasonable substation structure, and temperature change will rarely occur. Therefore, it is advised to adopt an underground powerhouse structure if the technical and geological circumstances allow for it. This will not only increase power generation head and efficiency, but also prevent it from being impacted by the ambient temperature, leading to increased thermal stress. Other hydraulic structures, such as arch dams, buttress dams, and sluices, should also take the impact of extreme weather into account in their design and safety checks due to global warming and the frequent occurrence of extreme weather. Extreme working conditions, such as cold waves and high-temperature flood discharge, can be calculated when numerical simulation is used to ensure the safe operation of buildings.

In essence, this overflow powerhouse structure can be simplified as a combination of large blocks (dam main body) and thin-walled bars (substation tunnel powerhouse). The impact of temperature change on the structure must be taken into account when similar structures are used in the future. Telescopic bars and structural joints can be used at the intersection of large blocks and thin-walled bars to ease pressure and thermal stress. However, this paper only provides a brief introduction to the repair scheme and compares a few repair schemes that have not undergone exhaustive numerical simulation and still lack theoretical backing. In order to make the suggested repair scheme more practical and affordable, it is necessary to simulate various repair schemes and determine the safety of the structure under various working conditions in the following stage of the research.

6. Conclusions

In this research, numerical simulation is largely utilized to investigate the reasons for fractures in the anti-arc portion of a concrete gravity dam in Guangdong Province, China, and the top of a substation tunnel. According to engineering knowledge and the dam's design data, a finite element model of the structure is created, and suitable calculation parameters are chosen, as well as simulated conditions for the dam's temperature and stress field distribution during regular operation and severe weather.

The findings demonstrate that the extensive fractures in the left section at the top of the substation tunnel are mostly caused by high summer temperatures and severe structural restrictions. Different areas' effects on thermal stress are deduced by lowering their linear expansion coefficients. According to the research, the jacking force created by the thermal expansion of the concrete on the right side of the substation tunnel, the drag force created by the thermal expansion of the concrete on the top of the substation tunnel, the self-weight of the concrete, and the water pressure created during water discharge all combine to create a tensile stress of about 1 MPa. As a consequence, when it is hot outside and there is a lot of water flowing, the tensile stress may reach 3 MPa, which is much higher than the tensile strength (1.5 MPa) and causes severe fractures. Wintertime temperature drops cause the overflow dam's surface concrete to experience cold shrinkage, which is restrained by the lower concrete and results in a tensile tension of around 1.6 MPa. As a result of the cold wave, the concrete temperature on the overflow surface fell at this time, causing further shrinkage. The tensile stress also rose to 4 MPa at this time, exceeding the tensile strength by 1.9 MPa and leading to horizontal connectivity cracks in the overflow surface's anti-arc section.

The simulation findings match the location of the fracture as it was actually found. The calculated fluctuation law of the stress field with temperature is compatible with crack gauge monitoring data for crack opening. These confirm the accuracy of the computation results and the soundness of the inferred explanations. This offers a fresh perspective on how to analyze the factors that lead to cracks in mass concrete, and similar structures can also take the effect of temperature into account. It also demonstrates the damaging effects of extreme weather on dams and other hydraulic structures, which calls for us to take these effects into account when designing and vetting the safety of future projects in order to minimize thermal stress and guarantee structural safety.

The combination of structural joints and expansion plates can be used for the composite structure of large blocks (dam main body) and thin-walled bars (substation tunnel powerhouse) to reduce the thermal stress of the structure, which serves as a model for the engineering design of similar structures.

The combination of structural cracks and expansion plates is suggested to lessen the structural restrictions of the overflow powerhouse based on the concept of thermal stress generation and engineering expertise. A combination of steel plate, structural adhesive, and anchor blot is suggested to treat the deep cracks at the top of the substation tunnel in light of the existing cracks in comparison to other repair schemes. To stop the corrosion of internal steel bars and structural leakage, various repair schemes are proposed in accordance with the cracks in the reverse arc section with different degrees of development. The research provides a reference for the design, monitoring, and repair of similar concrete gravity dams. Sadly, the repair scheme does not include any simulation verification. To ensure the viability and economy of the repair scheme, it is necessary to simulate various repair schemes and calculate the safety of the structure under various working conditions in the following stage of the research.

Author Contributions: Conceptualization, W.L.; Methodology, W.L., L.L., X.T., H.T. and C.Z.; Software, W.L., L.L. and X.T.; Validation, H.T.; Formal analysis, W.L.; Resources, H.T. and C.Z.; Writing—original draft, W.L., L.L. and X.T.; Project administration, C.Z. All authors have read and agreed to the published version of the manuscript.

Funding: This research was funded by Science and Technology Research Project of Jiangxi Education Department, grant number GJJ202020 and the Henan Province Science and Technology Research & Development Project, grant numbers cscec7b-2020-Z-14.

Data Availability Statement: Data will be made available on request.

Conflicts of Interest: The authors declare no conflict of interest.

References

1. Ruggeri, G. *Sliding Safety of Existing Gravity Dams-Final Report*; ICOLD European Club: Paris, France, 2004.
2. Goodman, R.E.; Ahlgren, C.S. Evaluating safety of concrete gravity dam on weak rock: Scott Dam. *J. Geotech. Geoenviron. Eng.* **2000**, *126*, 429–442. [CrossRef]
3. Riding, K.A. *Early Age Concrete Thermal Stress Measurement and Modeling*; The University of Texas at Austin: Austin, TX, USA, 2007.
4. Wu, S.; Huang, D.; Lin, F.-B.; Zhao, H.; Wang, P. Estimation of cracking risk of concrete at early age based on thermal stress analysis. *J. Therm. Anal. Calorim.* **2011**, *105*, 171–186. [CrossRef]
5. Malm, R.; Ansell, A. Cracking of Concrete Buttress Dam Due to Seasonal Temperature Variation. *ACI Struct. J.* **2011**, *108*, 51664198.
6. Ray, S.; Chandra Kishen, J. Fatigue crack growth due to overloads in plain concrete using scaling laws. *Sadhana* **2012**, *37*, 107–124. [CrossRef]
7. Chopra, A.K.; Chakrabarti, P. The Koyna earthquake and the damage to Koyna dam. *Bull. Seismol. Soc. Am.* **1973**, *63*, 381–397. [CrossRef]
8. Pekau, O.; Yuzhu, C. Failure analysis of fractured dams during earthquakes by DEM. *Eng. Struct.* **2004**, *26*, 1483–1502. [CrossRef]
9. Lin, P.; Guan, J.; Peng, H.; Shi, J. Horizontal cracking and crack repair analysis of a super high arch dam based on fracture toughness. *Eng. Fail. Anal.* **2019**, *97*, 72–90. [CrossRef]
10. Zhong, H.; Li, H.; Ooi, E.T.; Song, C. Hydraulic fracture at the dam-foundation interface using the scaled boundary finite element method coupled with the cohesive crack model. *Eng. Anal. Bound. Elem.* **2018**, *88*, 41–53. [CrossRef]
11. Tikka, J.; Hedman, R.; Silijander, A. Strain gauge capabilities in crack detection. In Proceedings of the 4th International Workshop on Structural Health Monitoring, New York, NY, USA, 10–11 June 2004; pp. 15–17.
12. Neild, S.; Williams, M.; McFadden, P. Development of a vibrating wire strain gauge for measuring small strains in concrete beams. *Strain* **2005**, *41*, 3–9. [CrossRef]
13. Saouma, V.E.; Anderson, D.Z.; Ostrander, K.; Lee, B.; Slowik, V. Application of fiber Bragg grating in local and remote infrastructure health monitoring. *Mater. Struct.* **1998**, *31*, 259–266. [CrossRef]
14. Jahanshahi, M.R.; Masri, S.F. A new methodology for non-contact accurate crack width measurement through photogrammetry for automated structural safety evaluation. *Smart Mater. Struct.* **2013**, *22*, 035019. [CrossRef]
15. Laefer, D.F.; Truong-Hong, L.; Carr, H.; Singh, M. Crack detection limits in unit based masonry with terrestrial laser scanning. *Ndt. E Int.* **2014**, *62*, 66–76. [CrossRef]
16. Tan, X.; Abu-Obeidah, A.; Bao, Y.; Nassif, H.; Nasreddine, W. Measurement and visualization of strains and cracks in CFRP post-tensioned fiber reinforced concrete beams using distributed fiber optic sensors. *Autom. Constr.* **2021**, *124*, 103604. [CrossRef]
17. Ren, Q.; Li, M.; Kong, T.; Ma, J. Multi-sensor real-time monitoring of dam behavior using self-adaptive online sequential learning. *Autom. Constr.* **2022**, *140*, 104365. [CrossRef]
18. Zhu, Y.; Tang, H. Automatic Damage Detection and Diagnosis for Hydraulic Structures Using Drones and Artificial Intelligence Techniques. *Remote Sens.* **2023**, *15*, 615. [CrossRef]

19. Sony, S.; Laventure, S.; Sadhu, A. A literature review of next-generation smart sensing technology in structural health monitoring. *Struct. Control Health Monit.* **2019**, *26*, e2321. [CrossRef]
20. Zhu, Y.; Xie, M.; Zhang, K.; Li, Z. A Dam Deformation Residual Correction Method for High Arch Dams Using Phase Space Reconstruction and an Optimized Long Short-Term Memory Network. *Mathematics* **2023**, *11*, 2010. [CrossRef]
21. Barpi, F.; Valente, S. Numerical simulation of prenotched gravity dam models. *J. Eng. Mech.* **2000**, *126*, 611–619. [CrossRef]
22. Sherard, J.L. *Embankment Dam Cracking*; Wiley (John) and Sons, Incorporated: Hoboken, NJ, USA, 1973.
23. Lin, P.; Zhou, W.; Liu, H. Experimental study on cracking, reinforcement, and overall stability of the Xiaowan super-high arch dam. *Rock Mech. Rock Eng.* **2015**, *48*, 819–841. [CrossRef]
24. Morin, P.B.; Léger, P.; Tinawi, R. Seismic behavior of post-tensioned gravity dams: Shake table experiments and numerical simulations. *J. Struct. Eng.* **2002**, *128*, 140–152. [CrossRef]
25. Carpinteri, A.; Valente, S.; Ferrara, G.; Imperato, L. Experimental and numerical fracture modelling of a gravity dam. In *Fracture Mechanics of Concrete Structures*; CRC Press: Boca Raton, FL, USA, 2003; pp. 351–360.
26. Perner, F.; Obernhuber, P. Analysis of arch dam deformations. *Front. Archit. Civ. Eng. China* **2010**, *4*, 102–108. [CrossRef]
27. Xu, W.; Qiang, S.; Hu, Z.; Ding, B.; Yang, B. Effect of hydration heat inhibitor on thermal stress of hydraulic structures with different thicknesses. *Adv. Civ. Eng.* **2020**, *2020*, 5029865. [CrossRef]
28. Lingye, L.; Zhang, C.; Pengfei, Z.; Tian, W. Influence of temperature rising inhibitor on temperature and stress field of mass concrete. *Case Stud. Constr. Mater.* **2023**, *18*, e01888. [CrossRef]
29. Bofang, Z. *Thermal Stresses and Temperature Control of Mass Concrete*; Elsevier Science & Technology: Saint Louis, MO, USA, 2013; p. 525.
30. Yunchuan, Z.; Liang, B.; Shengyuan, Y.; Guting, C. Simulation analysis of mass concrete temperature field. *Procedia Earth Planet. Sci.* **2012**, *5*, 5–12. [CrossRef]
31. Li, M.; Si, W.; Du, S.; Zhang, M.; Ren, Q.; Shen, Y. Thermal deformation coordination analysis of CC-RCC combined dam structure during construction and operation periods. *Eng. Struct.* **2020**, *213*, 110587. [CrossRef]
32. Léger, P.; Venturelli, J.; Bhattacharjee, S. Seasonal temperature and stress distributions in concrete gravity dams. Part 2: Behaviour. *Can. J. Civ. Eng.* **1993**, *20*, 1018–1029. [CrossRef]
33. Xu, W.; Zhang, C.; Liu, H.; Yang, J.; Wang, X.; Tian, W.; Cao, K.; Zhang, T. Simulation and analysis of corrosion fracture of reinforced concrete based on phase field method. *Case Stud. Constr. Mater.* **2022**, *17*, e01366. [CrossRef]